Quantum interpolation for high-resolution sensing

Citation: Ajoy, Ashok et al. "Quantum Interpolation for High-Resolution Sensing." Proceedings of the National Academy of Sciences 114, 9 (February 2017): 2149–2153 © 2017 National Academy of Sciences

As Published: http://dx.doi.org/10.1073/pnas.1610835114

Publisher: National Academy of Sciences (U.S.)

Persistent URL: http://hdl.handle.net/1721.1/111204

Version: Final published version: final published article, as it appeared in a journal, conference proceedings, or other formally published context

Quantum interpolation for high-resolution sensing

Ashok Ajoy[a,b], Yi-Xiang Liu[a,b], Kasturi Saha[a,b], Luca Marseglia[a,b], Jean-Christophe Jaskula[a,b], Ulf Bissbort[a,b,c], and Paola Cappellaro[a,b,1]

[a]Research Laboratory of Electronics, Massachusetts Institute of Technology, Cambridge, MA 02139; [b]Department of Nuclear Science & Engineering, Massachusetts Institute of Technology, Cambridge, MA 02139; and [c]Singapore University of Technology and Design, 487372 Singapore

Edited by Renbao Liu, The Chinese University of Hong Kong, Hong Kong, and accepted by Editorial Board Member Evelyn L. Hu November 28, 2016 (received for review July 2, 2016)

Recent advances in engineering and control of nanoscale quantum sensors have opened new paradigms in precision metrology. Unfortunately, hardware restrictions often limit the sensor performance. In nanoscale magnetic resonance probes, for instance, finite sampling times greatly limit the achievable sensitivity and spectral resolution. Here we introduce a technique for coherent quantum interpolation that can overcome these problems. Using a quantum sensor associated with the nitrogen vacancy center in diamond, we experimentally demonstrate that quantum interpolation can achieve spectroscopy of classical magnetic fields and individual quantum spins with orders of magnitude finer frequency resolution than conventionally possible. Not only is quantum interpolation an enabling technique to extract structural and chemical information from single biomolecules, but it can be directly applied to other quantum systems for superresolution quantum spectroscopy.

quantum sensing | quantum control | nanoscale NMR | NV centers

Precision metrology often needs to strike a compromise between signal contrast and resolution, because the hardware apparatus sets limits on the precision and sampling rate at which the data can be acquired. In some cases, classical interpolation techniques have become a standard tool to achieve a significantly higher resolution than the bare recorded data. For instance, the Hubble Space Telescope uses classical digital image processing algorithms like variable pixel linear reconstruction [Drizzle (1)] to construct a supersampled image from multiple low-resolution images captured at slightly different angles. Unfortunately, this classical interpolation method would fail for signals obtained from a quantum sensor, where the information is encoded in its quantum phase (2). Here we introduce a technique, which we call "quantum interpolation," that can recover the intermediary quantum phase, by directly acting on the quantum probe dynamics, and effectively engineer an interpolated Hamiltonian. Crucially, by introducing an optimal interpolation construction, we can exploit otherwise deleterious quantum interferences to achieve high fidelity in the resulting quantum phase signal.

Quantum systems, such as trapped ions (3), superconducting qubits (4, 5), and spin defects (6, 7) have been shown to perform as excellent spectrum analyzers and lock-in detectors for both classical and quantum fields (8–10). This sensing technique relies on modulation of the quantum probe during the interferometric detection of an external field. Such a modulation is typically achieved by a periodic sequence of π-pulses that invert the sign of the coupling of the external field to the quantum probe, leading to an effective time-dependent modulation $f(t)$ of the field (11–13). These sequences, more frequently used for dynamical decoupling (14, 15), can be described by sharp band-pass filter functions obtained from the Fourier transform of $f(t)$. This description lies at the basis of their application for precision spectroscopy, as the filter is well approximated by modified sinc functions, $F(\nu\tau, N) \approx \frac{\sin^2(4\pi N\nu\tau)}{\sin^2(4\pi\nu\tau)}$, where 2τ is the time interval between π-pulses, and N is the number of pulses. The filter passband is centered at $\nu = 1/(4\tau)$, its rejection (signal contrast) increases with the number of pulses as N^2, and the band-pass bandwidth (frequency resolution) decreases as $\Delta\nu = 1/(4N\tau)$, tremendously improving frequency resolution with increasing pulse numbers. Unfortunately, this high resolution can only be obtained if the experimental apparatus allows a correspondingly fine time sampling $\Delta\tau$, with a precision $1/(4N\nu)$. In practice, this is an extremely serious limitation, because conventional hardware sampling bounds are quickly saturated, leading to losses in both signal contrast and spectral resolution.

Our quantum interpolation technique can overcome these limitations in sensing resolution by capturing data points on a finer mesh than directly accessible due to experimental constraints, in analogy to classical interpolation. However, instead of interpolating the measured function values (which would contain no new information), the objective is to interpolate the ideal sensing evolution operator (propagator) in a coherent way. The key idea is presented in Fig. 1*A*. To achieve precision sensing at a desired frequency $\bar{\nu} = 1/4\bar{\tau}$, we use control sequences with different π-pulse separations, $\tau_k = k\Delta\tau$ and $\tau_{k+1} = (k+1)\Delta\tau$, where $\Delta\tau$ is the minimum timing step allowed by the hardware (and k is an integer). By combining different numbers of these building blocks, we can achieve an effective evolution for the desired time $N\bar{\tau} = (N-p)\tau_k + p\tau_{k+1}$ (where $0 \le p \le N$ is an integer). This result would be trivial if the effective Hamiltonian H during the pulsed evolution were constant, because $(e^{iH\tau_k})^{N-p}(e^{iH\tau_{k+1}})^p = e^{iHN\bar{\tau}}$. This simple prescription, however, hides the subtleties of our quantum interpolation scheme; indeed, the high-frequency resolution of dynamical decoupling sensing schemes arises exactly from the fact that the effective Hamiltonian does depend on the pulse timing. Then, extreme care must be taken in building the interpolated dynamics by a

Significance

Nanoscale magnetic resonance imaging enabled by quantum sensors is a promising path toward the outstanding goal of determining the structure of single biomolecules at room temperature. We develop a technique, which we name "quantum interpolation," to improve the frequency resolution of these quantum sensors far beyond limitations set by the experimental controlling apparatus. The method relies on quantum interference to achieve high-fidelity interpolation of the quantum dynamics between hardware-allowed time samplings, thus allowing high-resolution sensing. We demonstrate over two orders of magnitude resolution gains, and discuss applications of our work to high-resolution nanoscale magnetic resonance imaging.

Author contributions: A.A. and P.C. designed research; A.A., Y.-X.L., K.S., L.M., J.-C.J., U.B., and P.C. performed research; A.A., Y.-X.L., K.S., L.M., J.-C.J., U.B., and P.C. analyzed data; and A.A., Y.-X.L., K.S., L.M., J.-C.J., U.B., and P.C. wrote the paper.

The authors declare no conflict of interest.

This article is a PNAS Direct Submission. R.L. is a Guest Editor invited by the Editorial Board.

[1]To whom correspondence should be addressed. Email: pcappell@mit.edu.

This article contains supporting information online at www.pnas.org/lookup/suppl/doi:10.1073/pnas.1610835114/-/DCSupplemental.

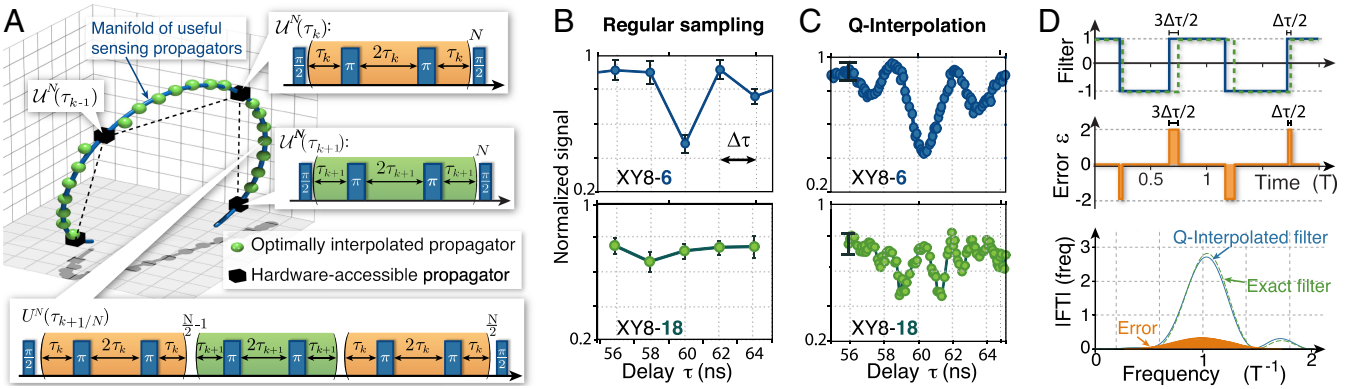

Fig. 1. Quantum Interpolation scheme. (*A*) Conceptual picture of quantum interpolation. The set of useful sensing propagators ($\mathcal{U}^N(\tau_{k+p/N})$, blue line) constitute a one-dimensional manifold in the 4D operator space, shown here in the dominant 3D subspace (see *SI Appendix, Quantum Interpolation: Theory & Practice, Geometric Representation*). Conventionally, the unitary evolution of a quantum sensor can only be probed at discrete intervals $\mathcal{U}^N(\tau_k)$ (black cubes), with $\tau_k = k\Delta\tau$, and classical signal interpolation would miss an accurate description (dashed black line). Quantum interpolation faithfully approximates the evolution ($U^N(\tau_{k+p/N})$, green spheres) by coherent combination of pulse sequences [*Insets*, CPMG (16) sequences], allowing for sampling at arbitrary small time intervals. (*B* and *C*) (*Top*) NMR signal from a single ^{14}N spin associated with the NV quantum sensor. (*B*) Sensing with conventional sequences limited to $\Delta\tau = 2$ ns. (*C*) Quantum interpolation, improving the resolution to 110 ps. (*Bottom*) Quantum interpolation can reveal details of the signal (the folding and reflection of the central peak leading to the double peak), as expected from the theoretical line shape at large pulse numbers (see *SI Appendix, Interferometric Spin Sensing via the NV Center*). (*D*) Filter function description of quantum interpolation. (*Top*) Time domain filter function $f(t)$ for the desired (dashed green lines) and interpolated pulse sequence (solid blue lines) for the simplest case of a half-time interpolation with total sequence time T. The deviation between these filters is the error function ϵ (shaded regions in *Middle*) that needs to be minimized for an optimal interpolation construction. (*Bottom*) Frequency domain representation of both filter functions and the Fourier Transform (FT) of their difference.

suitable ordering of the sequence blocks that will engineer the correct interpolated Hamiltonian.

Quantum Interpolation

Principles. The building blocks of the quantum interpolated dynamics are propagators $\mathcal{U}(\tau_k)$ describing the quantum probe evolution under a control sequence unit composed of π-pulses separated by a time $\tau_k = k\Delta\tau$. Experimentally, thus, we combine well-known control sequences such as the XY8 sequence (16–18). As shown in Fig. 1*A*, these operators $\mathcal{U}(\tau_k)$ can be thought of as a discrete subset of all of the possible propagators that one might want to access for quantum sensing. Combining sequences with different timings (Fig. 1*A*, *Inset*), we construct a propagator $U(\tau_{k+p/N})$ that approximates the desired interpolated dynamics, $\mathcal{U}(\tau_{k+p/N})$,

$$U^N(\tau_{k+p/N}) \equiv \mathcal{P}\left\{\prod_{m=1}^{N-p}\mathcal{U}(\tau_k)\prod_{n=1}^{p}\mathcal{U}(\tau_{k+1})\right\} \approx \mathcal{U}^N(\tau_{k+p/N}). \quad [1]$$

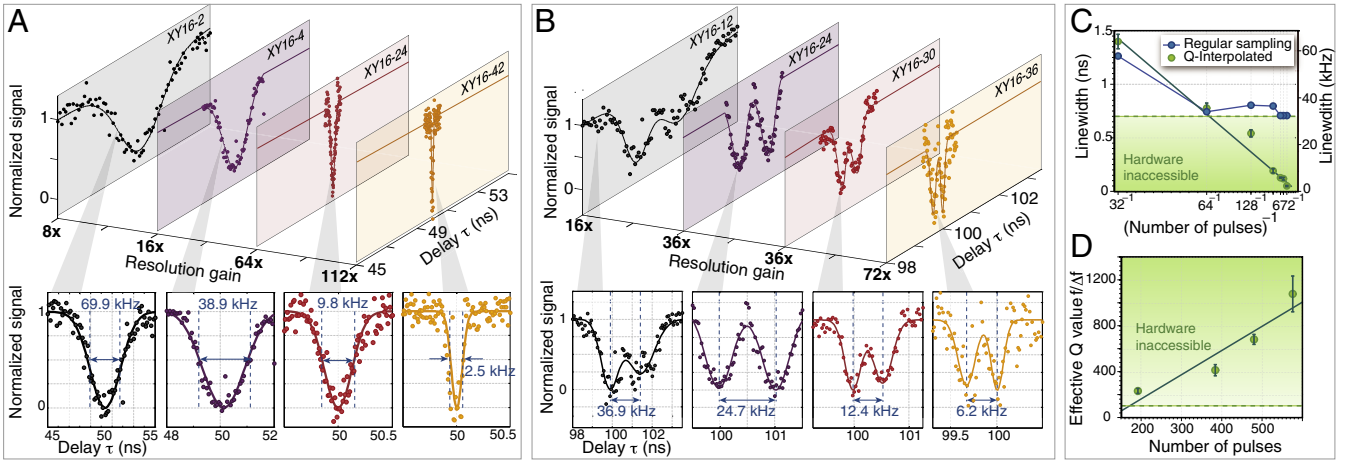

Fig. 2. High-resolution sensing and spectroscopy. (*A*) Detection of the spurious harmonic of an AC magnetic field via quantum-interpolated XY16 sequences. The incoherent external magnetic field is generated by an AC current at $f_{AC} = 2.5$ MHz through a 20-μm wire located in the vicinity of the NV center. Our hardware limitation ($\Delta\tau = 1$ ns) translates in a frequency resolution of $\Delta f_{AC} = 35.3$ kHz, and would cause a severe suppression of the detected signal as its linewidth decreases linearly with the number of π-pulses. In the rightmost image, quantum interpolation enables supersampling at 8.9 ps (an effective boost of 112), which still permits to resolve clearly a linewidth of 2.5 kHz. (*B*) Detection of incoherent AC magnetic fields with two distinct frequencies. Quantum interpolation with a maximum of 672 π-pulses allows for a resolution gain of a factor 72 and faithfully reconstructs the AC fields, even if the two frequencies are not resolved by regular XY16 sequences with our timing resolution. (*C*) Linewidth of the detected AC magnetometry signal (from *A*) with regular sampling (blue) and supersampling (green). The error bars are residuals to a Gaussian fit. (*D*) Sensing quality factor $Q = f/\Delta f$ extracted from *B*. Conventional dynamical decoupling sequences can only achieve $Q \lesssim 100$. This limit can be surpassed with quantum interpolation, scaling linearly with number of pulses, to reach $Q \approx 1{,}000$.

Here $\mathcal{P}$ describes a permutation of the propagators (the pulse sequence order). Only by optimizing $\mathcal{P}$, as explained in *Optimal Construction*, can we achieve high-fidelity quantum interpolation, which would be otherwise limited by errors caused by the noncommutativity of the dynamics and further amplified when considering a large number of pulses.

Before giving more details of the optimal construction, we demonstrate the need and advantages of quantum interpolation (Fig. 1 *B* and *C*) by performing high spectral resolution magnetometry using the electronic spin of the nitrogen vacancy (NV) center in diamond (19) as a nanoscale probe (7, 10, 20). Using a conventional XY8-6 dynamical decoupling sequence (17, 18) to measure the ^{14}N nuclear spin of the NV center, we obtain a low-resolution signal where the expected sinc-like dip is barely resolved (Fig. 1*B*). Upon increasing the number of pulses to XY8-18, this narrow dip is completely lost. To enhance the signal resolution, we use the optimized interpolation sequence that completely mitigates the deleterious effects of timing resolution and reveals the folding back of the dip into a double peak due to strong interference between the NV and the ^{14}N spin (Fig. 1*C* and *SI Appendix*, *Interferometric Spin Sensing via the NV Center*). Thanks to quantum interpolation, the number of points that can now be sampled scales linearly with the number of pulses N, and the resolution still improves as $1/N$. The sensing resolution is thus determined only by the quantum probe coherence time T_2 (simultaneously extended due to dynamical decoupling) and the number of pulses that can be reliably applied.

Optimal Construction. The ordering of the different pulse sequence blocks is a crucial step in achieving an interpolated propagator that remains the most faithful approximation of $\mathcal{U}^N(\tau_{k+p/N})$, even at large N. For instance, a naive construction, $\mathcal{P}=\mathbf{1}$ in Eq. **1**, would lead to fast error accumulation and the failure of quantum interpolation. We tackle this problem by minimizing the deviation $\epsilon(t)=|f_U(t)-f_{\mathcal{U}}(t)|$ of the filter function in the time domain (shaded regions in Fig. 1*D*) over the whole evolution. This procedure yields the optimal control sequence for any desired propagator, because we find that it also minimizes both the filter function error and the infidelity of the interpolated propagator, $U^N(\tau_{k+p/N})$, with the ideal one, $\mathcal{U}^N(\tau_{k+p/N})$. Intuitively, the optimal construction compensates the error at each decoupling sequence block, to achieve a constant error that does not depend on the number N of pulses and scales as $\Delta\tau$, allowing access to a large number of interpolated points. We show analytically and numerically that the errors for any interpolated propagator are approximately equal, and bounded by the error of $U^2(\tau_{k+1/2})=\mathcal{U}^2(\tau_{k+1/2})+\mathcal{O}(\Delta\tau^2)$ (see *SI Appendix*, *Optimal Quantum Interpolation Construction*).

Experimental Realization

Sensing Classical Fields. To demonstrate the power of quantum interpolation, we perform high-resolution magnetometry of a classical single-tone AC magnetic field at the frequency $f_{\mathrm{AC}}=2.5$ MHz. By applying optimally ordered quantum interpolated sequences (Fig. 2*A*), we detect the spurious harmonic (21) of frequency $2f_{\mathrm{AC}}$. As the number of π-pulses is increased, the filter function associated with the equivalent XY-N sequences, and, accordingly, the measured signal, becomes narrower. The signal linewidths are not affected by the finite time resolution, as highlighted in Fig. 2*C*. Without quantum interpolation, we reach our experimental resolution limit after applying a sequence of only 64 π-pulses (XY8-8 sequence; Fig. 1 *B* and *C*). Quantum interpolation enables AC magnetometry far beyond this limit: We obtain an improvement by a factor 112 in timing resolution, corresponding to a sampling time of 8.9 ps.

The advantage of quantum interpolation over conventional dynamical decoupling sequences is manifest when the goal is to resolve signals with similar frequencies. Fig. 2*B* shows that our quantum sensor is able to easily detect a classic dual-tone perturbation, resolving fields that are separated by $\Delta f=6.2$ kHz, far below the limit set by our native 1-ns hardware time resolution.

A useful figure of merit to characterize the resolution enhancement of quantum interpolation, in analogy to band-pass filters, is the Q value of the sensing peak, $Q=f/\Delta f$. The Q value for conventional decoupling pulse sequences is set by the finite time resolution, $Q=1/(2f\Delta\tau)$. Quantum interpolation lifts this constraint, allowing $Q\approx 2N/\pi$, limited only by the coherence time T_2, $N_{\max}\leq T_2/(2\tau)$, and pulse errors. Our experiments illustrate that the effective sensing Q can be linearly boosted with the pulse number to over 1,000 (Fig. 2*D*). Given typical NV coherence time (1 ms), π-pulse length (50 ns), and timing resolution (1 ns), an impressive increase of about 10^4 over the hardware limits is achievable. Quantum interpolation can also enhance alternative high-resolution sensing techniques like correlation spectroscopy (22), and Hartmann–Hahn sensing (23, 24) (see also *SI Appendix*, *Comparison with Other High-Resolution Sensing Techniques* for a detailed comparison with these methods).

Sensing Quantum Systems. Even more remarkably, the coherent construction of quantum interpolation ensures that one can measure not only classical signals, but also quantum systems [e.g., coupled spins (25)] with high spectral resolution. This result is nontrivial, because it implies that we are not only modulating the quantum sensor but also effectively engineering an interpolated Hamiltonian for the probed quantum system (26). Specifically, we consider a quantum probe coupled to the quantum system of interest via an interaction $\mathcal{H}=|0\rangle\langle 0|\mathcal{H}_0+|1\rangle\langle 1|\mathcal{H}_1$. Here $\mathcal{H}_{0,1}$ is the target system's Hamiltonian (of dimension D), which depends on which eigenstate $|0\rangle$, $|1\rangle$ the probe is in. Then, the propagator under a π-pulse

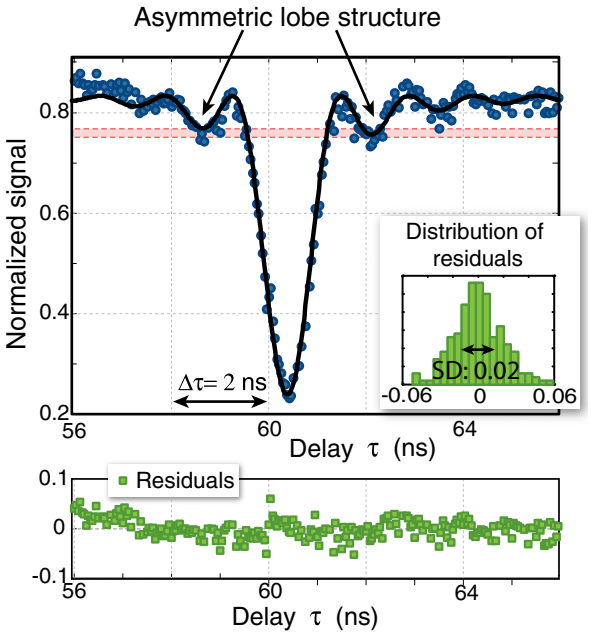

Fig. 3. High-resolution spin detection. A modified XY8-12 sequence enables an effective sampling at 48 ps (a 41-fold resolution gain with respect to the hardware-imposed $\Delta\tau$ = 2 ns). The lineshape of the ^{14}N NMR signal displays a slight asymmetry in the signal sidelobes, an expected feature (see *SI Appendix*, *Interferometric Spin Sensing via the NV Center*) of the NMR signal under the XY8 sequence (solid line). The agreement with the theory-fitted curve is very good, reflected by the relative residual SD being 3%.

train (with timings as in the XY8 sequence; Fig. 1*A*) is given by $\mathcal{U}^N(\tau) = |0\rangle\langle 0|\mathcal{U}_0^N(\tau) + |1\rangle\langle 1|\mathcal{U}_1^N(\tau)$, with

$$\mathcal{U}_{0,1}^N(\tau) = \left(e^{-i\mathcal{H}_{0,1}\tau} e^{-i\mathcal{H}_{1,0}2\tau} e^{-i\mathcal{H}_{0,1}\tau}\right)^N. \quad [2]$$

Sensing of the target quantum system is achieved via interference between the two evolution paths given by $\mathcal{U}_{0,1}^N(\tau)$, which results in the quantum probe signal $S = \left[1 + \mathrm{Tr}(\mathcal{U}_0^N \mathcal{U}_1^{N\dagger})/D\right]/2$ (27, 28). The interference is enhanced by increasing the number of pulses N, and by a careful choice of the time τ, making it susceptible once again to finite timing resolution. Quantum interpolation can overcome this limitation, engineering any propagator $U_{0,1}^N(\tau_{k+p/N}) \approx \mathcal{U}_{0,1}^N(\tau_{k+p/N})$ by suitably combining $\mathcal{U}_{0,1}^{N-p}(\tau_k)$ and $\mathcal{U}_{0,1}^p(\tau_{k+1})$. It is somewhat surprising that this construction would work: When considering a large number of pulses, one would expect that the noncommutativity of the propagators and the nonconvergence of the perturbative Baker–Campbell–Hausdorff expansion would amplify the discrepancy between ideal and interpolated propagator. Fortunately, the construction developed for classical fields still keeps the error small (as we show in *SI Appendix*, *Quantum Interpolation: Theory & Practice*) because higher-order terms cancel out in the interference between the propagators $U_{0,1}$.

Consider, for example, the coupling of a quantum probe (the NV center) to two-level systems (nuclear spins 1/2). NV centers implanted a few nanometers below the diamond surface have recently emerged as the prime technology toward the long-standing goal of obtaining high spatial resolution structure of single molecules in their natural environment, by performing nanoscale NMR spectroscopy (10, 17, 18, 29, 30). The outstanding key challenge is resolving the spectral features (and hence positions) of densely packed networks of spins in such molecules. Frequency differences, as small as a few Hertz, arise from chemical shifts and the coupling to the NV. The Hamiltonian of the jth spin in the molecule is given by $\mathcal{H}_0^{(j)} = \omega_L I_{zj}$; $\mathcal{H}_1^{(j)} = \omega_L I_{zj} + \sum_\nu A_{z\nu}^{(j)} I_{\nu j}$, where ω_L is the Larmor frequency of the spins, and $A_{z\nu}^{(j)}$ are the components of the coupling to the NV center. Then, the $\mathcal{U}_{0,1}$ propagators are composed of nuclear spin rotations conditioned on the NV state. For weakly coupled spins, the maximum interference signal arises at $\tau = \pi/\left(2\omega_L + A_{zz}^{(j)}\right)$, when the propagators correspond to rotations around two nonparallel axes separated by an angle $\alpha = arctan\left[A_{xx}^{(j)}/(\omega_L + A_{zz}^{(j)}/2)\right]$. The angle between the nuclear spin rotation axes in the two NV manifolds is amplified with every subsequent application of π-pulse, giving rise to a signal contrast that grows with N^2. The destructive interference is also amplified away from the sensing peak (27, 28), leading to a sinc linewidth that falls as $1/(4N\tau)$, similar to the results obtained using the semiclassical filter picture (see *SI Appendix*, *Interferometric Spin Sensing via the NV Center*).

To experimentally demonstrate the high-precision sensing reached by quantum interpolation, we measure the ^{14}N nuclear spin via its coupling to the NV center electronic spin. Even if the ^{14}N is strongly coupled to the NV ($A_{zz} = -2.16$ MHz), it usually does not give rise to an interferometric signal because of its transverse coupling $A_{zx} = 0$. However, a small perpendicular field $B_\perp = 0.62$ G generates an effective transverse coupling $\gamma_e B_\perp A_{xx}/(\Delta_0 - \gamma_e B_z)$, with $A_{xx} = -2.62$ MHz (31) and $\gamma_e = 2.8$ MHz/G as the NV gyromagnetic ratio. This effect becomes sizable at a longitudinal magnetic field $B_z = 955.7$ G that almost compensates the NV zero-field splitting $\Delta_0 = 2.87$ GHz. The ^{14}N nuclear spin frequency is largely set by its quadrupolar interaction $P = -4.95$ MHz, a high frequency beyond our timing resolution (Fig. 1*B*). We used quantum interpolation to supersample the signal at 48 ps (a 41-fold resolution gain), revealing precise features of the spectral lineshape (Fig. 3), including the expected slight asymmetry in sidelobes (*SI Appendix*, *Interferometric Spin Sensing via the NV Center*). Detecting this distinct spectral feature confirms that quantum interpolation can, indeed, achieve a faithful measurement of the quantum signal, as we find an excellent match of the experimental data with the theoretical model, with the error being less than 3% for most interpolated points. The ability to probe the exact spectral lineshape provides far more information than just the signal peaks, especially when there could be overlapping peaks or environment-broadened linewidths.

Conclusion and Outlook

These results have immediate and far-reaching consequences for nanoscale NV NMR (9, 10, 32), where our technique can map spin arrangements of a nearby single protein with a spatial resolution that dramatically improves with the number of pulses. The Q value provides an insightful way to quantify the resolution gains for these applications. With a $Q \approx 10^4$ that is currently achievable, ^{13}C chemical shifts of aldehyde and aromatic groups can now be measured (33). Beyond sensing nuclear spins, we envision quantum interpolation to have important applications in condensed matter, to sense high-frequency (hence high Q) signals (34), such as those arising from the excitation of spin-wave modes in magnetic materials like yittrium iron garnett (35).

In conclusion, we have developed a quantum interpolation technique that achieves substantial gains in quantum sensing resolution. We demonstrated its advantages by performing high-frequency-resolution magnetometry of both classical fields and single spins using NV centers in diamond. The technique allows pushing spectral resolution limits to fully exploit the long coherence times of quantum probes under decoupling pulses. Quantum interpolation could also enhance the performance of other NV-based sensing technique. We experimentally demonstrated resolution gains of 112, and Q-value gains of over 1,000, although the ultimate limits of the technique can be at least an order of magnitude larger. Quantum interpolation thus turns quantum sensors into high-resolution and high-Q spectrum analyzers of classical and quantum fields. We expect quantum interpolation to be an enabling technique for nanoscale single-molecule spectroscopy at high magnetic fields (36), allowing the discrimination of chemical shifts and angstrom-resolution single-molecule structure.

ACKNOWLEDGMENTS. We thank E. Bauch, F. Casola, D. Glenn, F. Jelezko, S. Lloyd, M. Lukin, E. Rosenfeld, and R. Walsworth for stimulating discussions and careful reading of the manuscript. This work was supported, in part, by the US Army Research Office through Grants W911NF-11-1-0400 and W911NF-15-1-0548 and by the NSF Grant PHY0551153 (Center for Ultracold Atoms).

1. Fruchter A, Hook RN (1997) Novel image-reconstruction method applied to deep Hubble Space Telescope images. *Proc SPIE* 3164:120.
2. Giovannetti V, Lloyd S, Maccone L (2006) Quantum metrology. *Phys Rev Lett* 96(1):010401.
3. Kotler S, Akerman N, Glickman Y, Keselman A, Ozeri R (2011) Single-ion quantum lock-in amplifier. *Nature* 473(7345):61–65.
4. Yan F, et al. (2012) Spectroscopy of low-frequency noise and its temperature dependence in a superconducting qubit. *Phys Rev B* 85:174521.
5. Bylander J, et al. (2011) Noise spectroscopy through dynamical decoupling with a superconducting flux qubit. *Nat Phys* 7:565–570.
6. Álvarez GA, Suter D (2011) Measuring the spectrum of colored noise by dynamical decoupling. *Phys Rev Lett* 107:230501.
7. Bar-Gill N, et al. (2012) Suppression of spin-bath dynamics for improved coherence of multi-spin-qubit systems. *Nat Commun* 3:858.
8. Romach Y, et al. (2015) Spectroscopy of surface-induced noise using shallow spins in diamond. *Phys Rev Lett* 114:017601.
9. Shi F, et al. (2015) Single-protein spin resonance spectroscopy under ambient conditions. *Science* 347(6226):1135–1138.
10. Lovchinsky I, et al. (2016) Nuclear magnetic resonance detection and spectroscopy of single proteins using quantum logic. *Science* 351(6275):836–341.

11. Cywinski L, Lutchyn RM, Nave CP, DasSarma S (2008) How to enhance dephasing time in superconducting qubits. *Phys Rev B* 77(17):174509.
12. Ajoy A, Álvarez GA, Suter D (2011) Optimal pulse spacing for dynamical decoupling in the presence of a purely dephasing spin bath. *Phys Rev A* 83:032303.
13. Smith PES, Bensky G, Álvarez GA, Kurizki G, Frydman L (2012) Shift-driven modulations of spin-echo signals. *Proc Natl Acad Sci USA* 109(16):5958–5961.
14. Viola L, Knill E, Lloyd S (1999) Dynamical decoupling of open quantum systems. *Phys Rev Lett* 82(12):2417–2421.
15. de Lange G, Wang ZH, Riste D, Dobrovitski VV, Hanson R (2010) Universal dynamical decoupling of a single solid-state spin from a spin bath. *Science* 330(6000):60–63.
16. Carr HY, Purcell EM (1954) Effects of diffusion on free precession in nuclear magnetic resonance experiments. *Phys Rev* 94(3):630–638.
17. Staudacher T, et al. (2013) Nuclear magnetic resonance spectroscopy on a (5-nanometer)3 sample volume. *Science* 339(6119):561–563.
18. Mamin HJ, et al. (2013) Nanoscale nuclear magnetic resonance with a nitrogen-vacancy spin sensor. *Science* 339(6119):557–560.
19. Taylor JM, et al. (2008) High-sensitivity diamond magnetometer with nanoscale resolution. *Nat Phys* 4(10):810–816.
20. Myers BA, et al. (2014) Probing surface noise with depth-calibrated spins in diamond. *Phys Rev Lett* 113(2):027602.
21. Loretz M, et al. (2015) Spurious harmonic response of multipulse quantum sensing sequences. *Phys Rev X* 5:021009.
22. Laraoui A, Meriles CA (2013) Approach to dark spin cooling in a diamond nanocrystal. *ACS Nano* 7(4):3403–3410. PMID: 23565720.
23. Belthangady C, et al. (2013) Dressed-state resonant coupling between bright and dark spins in diamond. *Phys Rev Lett* 110:157601.
24. London P, et al. (2013) Detecting and polarizing nuclear spins with double resonance on a single electron spin. *Phys Rev Lett* 111:067601.
25. Sushkov AO, et al. (2014) All-optical sensing of a single-molecule electron spin. *Nano Lett* 14(11):6443–6448.
26. Ajoy A, Cappellaro P (2013) Quantum simulation via filtered Hamiltonian engineering: Application to perfect quantum transport in spin networks. *Phys Rev Lett* 110:220503.
27. Taminiau TH, et al. (2012) Detection and control of individual nuclear spins using a weakly coupled electron spin. *Phys Rev Lett* 109(13):137602.
28. Kolkowitz S, Unterreithmeier QP, Bennett SD, Lukin MD (2012) Sensing distant nuclear spins with a single electron spin. *Phys Rev Lett* 109:137601.
29. Loretz M, Pezzagna S, Meijer J, Degen CL (2014) Nanoscale nuclear magnetic resonance with a 1.9-nm-deep nitrogen-vacancy sensor. *Appl Phys Lett* 104(3):033102.
30. Rugar D, et al. (2015) Proton magnetic resonance imaging using a nitrogen-vacancy spin sensor. *Nat Nanotechnol* 10(2):120–124.
31. Chen M, Hirose M, Cappellaro P (2015) Measurement of transverse hyperfine interaction by forbidden transitions. *Phys Rev B* 92:R020101.
32. Ajoy A, Bissbort U, Lukin MD, Walsworth RL, Cappellaro P (2015) Atomic-scale nuclear spin imaging using quantum-assisted sensors in diamond. *Phys Rev X* 5:011001.
33. Ernst RR, Bodenhausen G, Wokaun A (1987) *Principles of Nuclear Magnetic Resonance in One and Two Dimensions* (Clarendon, Oxford).
34. van der Sar T, Casola F, Walsworth R, Yacoby A (2015) Nanometre-scale probing of spin waves using single electron spins. *Nat Commun* 6:7886.
35. Serga AA, Chumak AV, Hillebrands B (2010) YIG magnonics. *J Phys D Appl Phys* 43(26):264002.
36. Hemmer P (2013) Toward molecular-scale MRI. *Science* 339(6119):529–530.

Supplementary Information: Quantum Interpolation for High Resolution Sensing

A. Ajoy[a], **Y. X. Liu**[a], **K. Saha**[a], **L. Marseglia**[a], **J.-C. Jaskula**[a], **U. Bissbort**[a,b], **and P. Cappellaro**[a, 1]

[a]Research Laboratory of Electronics and Department of Nuclear Science & Engineering, Massachusetts Institute of Technology, Cambridge, MA; [b]Singapore University of Technology and Design, 487372 Singapore

Contents

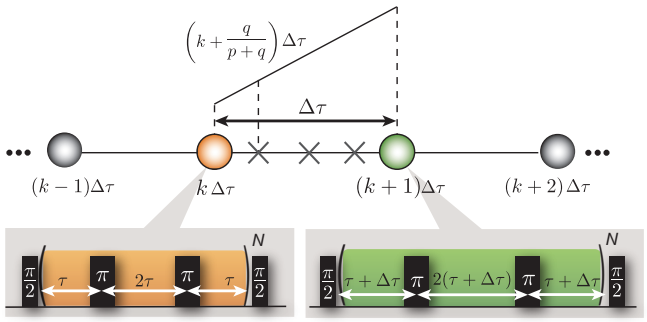

Fig. S1. Schematic of quantum interpolation based supersampling. Consider that we have, due to hardware limitations, a sampling resolution $\Delta\tau$ in the delays τ that are swept in the usual CPMG sequence. If $\Delta\theta = \omega_L\Delta\tau$ this refers to the fact that one can only sample angles $k\Delta\theta$, with integral k (purple points). The aim of quantum interpolation based supersampling is to effectively obtain a large number of samples $\left(k+\frac{q}{p+q}\right)\Delta\theta$ (crosses) between two neighboring hardware allowed samples. In principle for N cycles of a CPMG sequence, the number of experimentally achievable samples with low error scales $\propto N$, allowing the effective sensing resolution to be limited only by the number of pulses that can be reliably applied.

1. Quantum Interpolation: Theory & Practice

The key power of the interferometric CPMG spin sensing protocol is that as the number of cycles N increases the signal strength increases $\propto N^2$ and the linewidth falls as $w \propto 1/N$, yielding the double advantages of higher sensitivity and higher resolution for increasing number of pulses. To achieve the goal of high sensitivity spin sensing, we need to apply the sensing protocol in its optimal conditions, that is, at large N and high field (high frequency ω_L). Indeed, at high field, one also gains additionally in sensitivity and resolution because of an increase in polarization of the nuclear spins being sensed [1], and the fact that parameters of interest like chemical shifts scale with magnetic field, thereby allowing an effective gain in sensing resolution.

However, in real experiment finite hardware sampling rate limits the timing resolution, which doesn't allow us to sample the sensing peak efficiently. Quantum interpolation overcomes hardware finite-timing resolution limits to dramatically gain in both sensitivity and resolution.

1.1. Theory of quantum interpolation. The simplest instance of quantum interpolation can be obtained by combining two evolution blocks, with successive time intervals, τ_k and

[1]To whom correspondence should be addressed. E-mail: pcappell@mit.edu.

$\tau_{k+1} = \tau_k + \Delta\tau$, to obtain the intermediate evolution at $\tau_k + \Delta\tau/2$ (Fig. S1 and Fig. 1**A** in main paper). Before considering more complex situations (and in particular their optimal construction), we analyze in details this simple case. While the construction could be applied more broadly to any pair of different-time propagators, here we will focus on the evolution operators arising from quantum sensing of AC-fields or quantum fields by a single quantum probe. This dynamics has been studied in details before (see for example Refs. [2–4]), and the main result can be summarized by stating that the signal arises from the different evolution paths in the two manifolds defined by the qubit probe, $S = \frac{1}{2}\mathrm{Tr}\left[\mathcal{U}^{\dagger}_{|0\rangle}(\tau)\mathcal{U}_{|-1\rangle}(\tau)\right]$. Here the propagators $\mathcal{U}_{|i\rangle}(\tau)$ describe the evolution of the target systems in each manifold of the quantum probe, $|i\rangle$, that is determined by Hamiltonians $\mathcal{H}_{|i\rangle}(\tau)$. While these effective Hamiltonians are time-independent over the given evolution time, their form does depend on the duration of the evolution itself. Only at special times (that depend on the target system) there is substantial (destructive) interference that yields the maximum signal contrast. For completeness, we present a detailed description of these results in Sec. 6.

Quantum interpolation has the goal to engineer $\mathcal{H}(\tau)$ that precisely map out the signal at all times. For example, we can define the interpolated propagator

$$U(\tau_k + \Delta\tau/2) \equiv [\mathcal{U}(\tau_k)\mathcal{U}(\tau_k + \Delta\tau)]^{1/2} \quad [1]$$

A good quantum interpolation construction ensures that this propagator is a faithful approximation of the desired $\mathcal{U}(\tau_k + \Delta\tau/2) = \exp[-i(\tau_k + \Delta\tau/2)\mathcal{H}(\tau_k + \Delta\tau/2)]$. In the context of quantum sensing, however, the desired condition for a good approximation is that the interferometric signal is preserved to second order in $\Delta\tau$:

$$\mathrm{Tr}\left\{U^2_{|0\rangle}(\tau_k + \Delta\tau/2)U^{2\dagger}_{|-1\rangle}(\tau_k + \Delta\tau/2)\right\} = \quad [2]$$
$$\mathrm{Tr}\left\{\mathcal{U}^2_{|0\rangle}(\tau_k + \Delta\tau/2)\mathcal{U}^{2\dagger}_{|-1\rangle}(\tau_k + \Delta\tau/2)\right\} + \mathcal{O}(\Delta\tau^2)$$

Generalizing this simple example, while hardware limits us only to sample $k\Delta\tau$ and $(k+1)\Delta\tau$, quantum interpolation allows us to *linearly* interpolate the quantum probe dynamics over the interval $\Delta\tau$, so that the signal effectively supersamples points $\left(k + \frac{q}{p+q}\right)\Delta\tau$ (Fig. S1). Given $2N$ π-pulses in the spin sensing sequence, this can expressed as,

$$U^N\left[\left(k + \frac{q}{p+q}\right)\Delta\tau\right] \equiv [U^p(k\Delta\tau)U^q((k+1)\Delta\tau)]^{\frac{N}{p+q}}$$
$$\approx \mathcal{U}_0^N\left[\left(k + \frac{q}{p+q}\right)\Delta\tau\right] \quad [3]$$

Importantly, as N increases, the number of points $q/(p+q)$ that can be supersampled ideally scales $\propto N$. This is remarkable because although the linewidth decreases $\propto 1/N$, the interpolated resolution scales $\propto N$, allowing one to completely mitigate the deleterious effects of timing resolution $\Delta\tau$. The sensing resolution is now determined only the number of pulses that can be reliably applied, and the NV coherence time T_2, and experimental gains in resolution approaching three orders of magnitude are now achievable. However, for the success of quantum interpolation it is crucial that the approximation in Eq. (3) is good even for an increasing number of pulses. This is a non-trivial task that we accomplish by developing an optimal quantum interpolation construction, as explained in details in Sec. 3. Before introducing the optimal construction, we discuss the sources of infidelity at the level of the simplest interpolated propagator, as in Eq. (1).

1.2. Quantum Interpolation for Sensing. We now restrict our analysis of quantum interpolation to sensing via Dynamical Decoupling (DD) protocols [2]. While in the standard protocols the signal is obtained by sweeping the interpulse delay in steps $\Delta\tau$ set by hardware limitations, quantum interpolation can achieve higher resolution by combining DD pulse sequence blocks with unequal timings.

We consider the scenario where the quantum probe (e.g. a single NV center in diamond) is used to detect a nearby nuclear spin. Optimal contrast is then found when the inter-pulse delay exactly matches the effective resonance frequency ω of the nuclear spin, which depends both on the external magnetic field and -critically- on the coupling to the NV spin itself (see Sec. 6.1). That is, the largest signal contrast is achieved for $2\tau\omega = \pi$, but this might not be achievable in practice due to hardware limitations, leading to a loss in signal contrast and resolution (see Sec. 4.1). To simplify the notation, we will use the dimensionless time (angle) $\theta = 2\omega\tau$ and its sampling step $\Delta\theta = 2\omega\Delta\tau$.

Assume first that due to finite sampling, we can only achieve the angles $\pi \pm \Delta\theta/2$, while the maximum contrast would be achieved at $\theta = \pi$. We can use quantum interpolation as in Eq. (1) to achieve the desired angle, while keeping a large number of pulses for high resolution:

$$U^N_{|i\rangle}(\pi) = \left[\mathcal{U}_{|i\rangle}(\pi + \Delta\theta/2)\mathcal{U}_{|i\rangle}(\pi - \Delta\theta/2)\right]^{N/2}. \quad [4]$$

Here we describe the effective propagator in each of the NV manifolds ($|i\rangle = \{|0\rangle, |-1\rangle\}$) that can be obtained by a sequence with unequally spaced pulses (see also Fig. 1.**A** of the main paper). Using the results in Ref. [2–4] (also re-derived in Sec. 6) we can evaluate the interpolated propagators to second order in $\Delta\theta$:

$$\left[\mathcal{U}_{|0\rangle}(\pi + \Delta\theta/2)\mathcal{U}_{|0\rangle}(\pi - \Delta\theta/2)\right]^{N/2} \approx \quad [5]$$
$$\cos(N\alpha_j)\mathbb{1} - i\frac{\sin(N\alpha_j)}{\sin(2\alpha_j)}\boldsymbol{\sigma}\cdot$$
$$\left[\hat{\mathbf{n}}_{1_\perp}(2\cos(\alpha'_j)\sin\alpha_j) + \Delta\theta\sin\alpha_j(1+\cos\alpha_j)(\hat{\mathbf{n}}_{1_\perp}\times\hat{\mathbf{n}}_1)\right]$$

$$\left[\mathcal{U}_{|-1\rangle}(\pi + \Delta\theta/2)\mathcal{U}_{|-1\rangle}(\pi - \Delta\theta/2)\right]^{N/2} \approx \quad [6]$$
$$\cos(N\alpha_j)\mathbb{1} + i\frac{\sin(N\alpha_j)}{\sin(2\alpha_j)}\boldsymbol{\sigma}\cdot$$
$$\left[\hat{\mathbf{n}}_{0_\perp}(2\cos(\alpha'_j)\sin\alpha_j) + \Delta\theta\sin\alpha_j(1+\cos\alpha_j)(\hat{\mathbf{n}}_{0_\perp}\times\hat{\mathbf{n}}_0)\right]$$

where we used the definitions:

$$\hat{\mathbf{n}}_{1_\perp} = -\frac{\hat{\mathbf{n}}_0 - \hat{\mathbf{n}}_1\cos\alpha_j}{\sin\alpha_j} \quad [7]$$

$$\hat{\mathbf{n}}_{0_\perp} = \frac{\hat{\mathbf{n}}_1 - \hat{\mathbf{n}}_0\cos\alpha_j}{\sin\alpha_j} \quad [8]$$

$$\sin^2\alpha'_j = \sin^2\alpha_j + \Delta\theta^2(1+\cos\alpha_j)^2. \quad [9]$$

Here the angle $\alpha_j = \tan^{-1}\left[\frac{A^{(j)}_{zx}}{\omega_L + A^{(j)}_{zz}}\right]$ and vectors $\hat{\mathbf{n}}_0 = \mathbf{z}$, $\hat{\mathbf{n}}_1 = \cos(\alpha_j)\mathbf{z} + \sin(\alpha_j)[\cos(\phi_j)\mathbf{x} + \sin(\phi_j)\mathbf{y}]$ are determined by

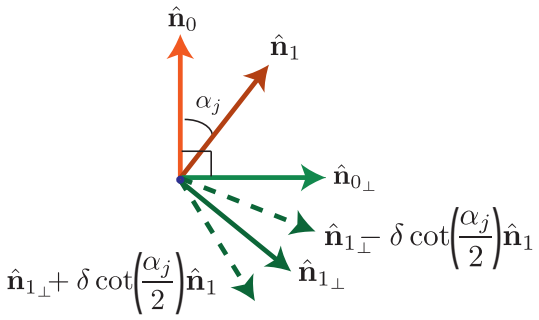

Fig. S2. Compensation mechanism in quantum interpolation of $U(\tau_k + \Delta\tau/2)$. Compensation mechanism in the construction of the quantum interpolated half-way point $U(\tau_k + \Delta\tau/2)$. We denote the two effective axes corresponding to the operators $\mathcal{U}_{|0\rangle}$ and $\mathcal{U}_{|-1\rangle}$ in Eq. (36). Here the red arrows refer to the original nuclear axes $\hat{\mathbf{n}}_0$ and $\hat{\mathbf{n}}_1$ conditioned on the state of the NV, separated by the tilt angle α_j. As a result of the CPMG sequence, these axes respectively effectively become $\hat{\mathbf{n}}_{0_\perp}$ and $\hat{\mathbf{n}}_{1_\perp}$ (green arrows). To describe the linewidth of the sensing signal one notices that the propagator $\mathcal{U}_{|0\rangle}(\pi \pm \delta)$ (Eq. 45) are effectively described by the vectors $\hat{\mathbf{n}}_{1_\perp} \mp \delta \cot\left(\frac{\alpha_j}{2}\right)\hat{\mathbf{n}}_1$ (dashed green arrow), and the product $[\mathcal{U}_{|0\rangle}(\pi + \delta)\mathcal{U}_{|0\rangle}(\pi - \delta)]$ points in the direction $\hat{\mathbf{n}}_{1_\perp}$ to second order in δ, forming the basis of quantum interpolation.

the hyperfine parameters A^j_{zz}, A^j_{zx} and the Larmor frequency ω_L of the target spin.

Remarkably, when combining these propagators to obtain the interferometric signal, the dependence of α'_j on $\Delta\theta$ is removed and the signal approaches more closely the desired dip. The sensing signal as a function of $\Delta\theta$ is now

$$\begin{aligned} S &= \cos^2(N\alpha_j) - \sin^2(N\alpha_j)\cos\alpha_j \\ &- \frac{\sin^2(N\alpha_j)}{\sin^2(2\alpha_j)}\left[\Delta\theta^2 \sin^2\alpha_j\,(1+\cos\alpha_j)^2\,(1-\cos\alpha_j)\right]. \end{aligned} \quad [10]$$

The first line is exactly the signal magnitude obtained at the signal peak – but now the width is set weakly by the second line that goes as $\Delta\theta^2$, which is responsible for the loss of signal contrast. Quantum interpolation thus compensates the deleterious effects on the signal contrast that derives from not being able to exactly set the optimal time $\theta = \pi$ (see also Sec. 4.1). This compensation mechanism has a simple geometric interpretation (Fig. S2) – similar to a spin echo [5], the linear dependence on $\Delta\theta$ leading to the destructive interference in Eq. (46) is removed by employing another vector with the opposite sign, giving an effective propagator that is independent of $\Delta\theta$.

We note that while in the above analysis we considered the case where the hardware can sample the signal at angles symmetric with respect to $\theta = \pi$, , we can also numerically evaluate that the quantum interpolation construction in Eq. (4) is robust even when we can only sample at times $\theta = \pi + \delta_0 \pm \Delta\theta/2$. This is shown in Fig. S3, where we plot the signal as a function of $\Delta\theta$ for different δ_0. It is evident that for any slice in the δ_0 dimension, the signal falls off quadratically in $\Delta\theta$, a reflection of the fact that to first order the quantum interpolation compensation mechanism (Fig. S2) is still robust.

1.3. Evaluating the fidelity of quantum interpolation. While we are mostly interested in the final interferometric signal from the quantum probe, we can also directly evaluate the fidelity of the interpolated propagators. Using a trace norm as a measure of fidelity [6], we show that the fidelity is one to second order in $\Delta\theta$. The ideal propagator is $U_{id} = \mathcal{U}^2_{|0\rangle}(\pi) = \exp(-i2\alpha_j\sigma\cdot\hat{\mathbf{n}}_{1\perp})$.

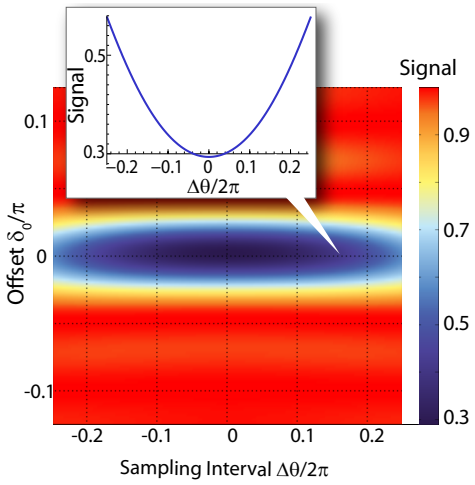

Fig. S3. Robustness of quantum interpolation to a timing offset δ_0. We consider the signal obtained using the quantum interpolated unitary $\left[\mathcal{U}_{|i\rangle}(\pi + \delta_0 + \Delta\theta/2)\mathcal{U}_{|i\rangle}(\pi + \delta_0 - \Delta\theta/2)\right]^{N/2}$, for different values of δ_0. We numerically calculate the signal with $\alpha_j = 0.1$ rad following Eq. (43). The graph indicates, as expected from Eq. (2), that the interpolated unitary faithfully produces the same signal as the target unitary $\mathcal{U}(\pi + \delta_0)$ independent of the choice of δ_0. Moreover, the deviation in the signal is second order in $\Delta\theta$ (inset).

Comparing with the quantum interpolated expression, we have that the trace norm,

$$\begin{aligned} F &= \mathrm{Tr}\left\{\mathcal{U}_{|0\rangle}(\pi + \Delta\theta/2)\mathcal{U}_{|0\rangle}(\pi - \Delta\theta/2)U^\dagger_{id}\right\} \\ &= \cos(2\alpha_j)\left[\sin^2(\Delta\theta/2) + \cos^2(\Delta\theta/2)\cos(2\alpha_j)\right] \\ &+ 2\sin(2\alpha_j)\,\sin\alpha_j\,\cos(\alpha'_j)\cos(\Delta\theta/2) \\ &\approx 1 + \mathcal{O}(\Delta\theta^2) \end{aligned} \quad [11]$$

Note that except the $\cos(\alpha'_j)$ term, all the other terms are second order or higher in $\Delta\theta$. The $\cos(\alpha'_j)$ term too is weighted by $\sin^2\alpha_j$, and for most practical cases of spin sensing, where α_j is small, this term has a negligible contribution. Hence to a very good approximation, the quantum interpolation expression is good to first order in $\Delta\theta$.

We can also evaluate experimentally the fidelity of quantum interpolation by comparing the signal obtained from the usual hardware-limited sampling with an interpolation construction that assume a larger bound in time sampling: that is, we deliberately undersample the signal and recover it by quantum interpolation. The results are shown in Fig. S4. We construct the propagators,

$$[U^p_i(k\Delta\theta + \delta)U^q_i((k+p+q)\Delta\theta + \delta)]^{\frac{N}{p+q}} \approx \mathcal{U}^N_i[(k+q)\Delta\theta + \delta] \quad [12]$$

Both the left and right hand sides of the equation can be independently constructed experimentally. If the approximation fidelity in Eq. (12) is good, the signals should be identical in both cases. The experimental results show a very good overlap, demonstrating that the construction error is low for most values of (p, q). However, the error is found to slightly increase away from the sensing peak. This is an artifact of the construction of Eq. (12), which is non-optimal. In particular, the approximation becomes worse when $p \approx q \approx N/2$, as already shown by Eq. (3), where the error grows with N and δ. These errors can be compensated by using an optimal construction, which is a key ingredient to our quantum interpolation scheme.

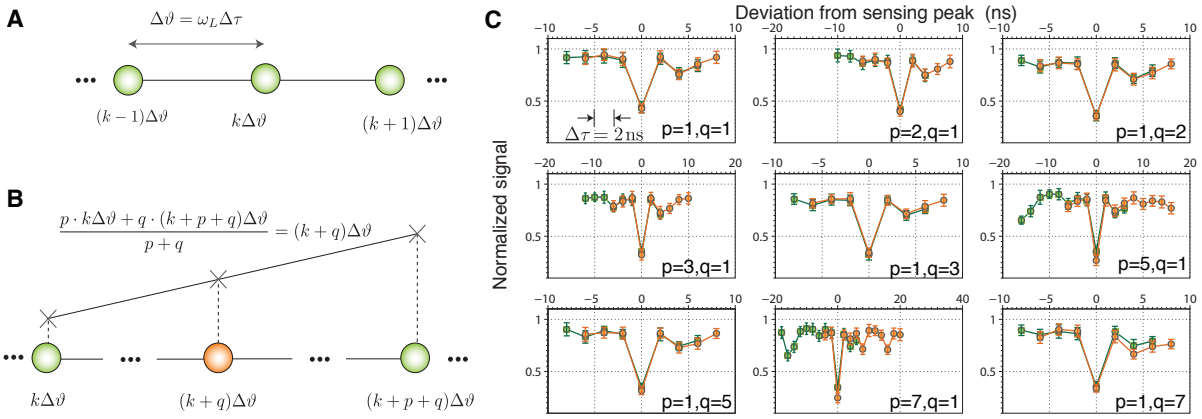

Fig. S4. Experimental fidelity of quantum interpolation. In these experiments, we deliberately undersample the signal from a ^{14}N spin using a timing resolution that is larger than the intrinsic $\Delta\tau = 2$ns set by hardware. The experiments are schematically described in **(A-B)**. In **(C)**, we construct for different values of (p, q) (the legend shows $q/(p+q)$) in an XY8-6 sequence, the approximate supersampled point $U^N((k+q)\Delta\theta+\delta) \equiv [\mathcal{U}^p(k\Delta\theta+\delta)\mathcal{U}^q((k+p+q)\Delta\theta+\delta)]^{N/(p+q)}$ (orange circles) and compare it against the ideal one $\mathcal{U}^N((k+q)\Delta\theta+\delta)$ (green circles). Both these propagators can be separately and individually constructed experimentally, allowing us to characterize the supersampling error with no free parameters (i.e. model independent). In these experiments k is swept, and the sensing peak corresponds to the closest value of k such that $k\Delta\theta \approx \pi$. If the construction has high fidelity error than the two lines should be identical and shifted, and hence should overlap in the panels. The results demonstrate that the construction error is low for most values of (p, q), and this can be further improved by means of an optimal interpolation construction (see Sec. 3).

1.4. Comparison with Baker-Campbell-Hausdorff result.

The effectiveness of the quantum interpolation construction cannot be seen as a simple manifestation of the zeroth order Baker-Campbell-Hausdorff (BCH) expansion [7, 8]. The zeroth order BCH expression does not care for cross terms or commutators between the two unitaries, and can be written down as, $\left[\mathcal{U}_{|0\rangle}(\pi+\Delta\theta/2)\mathcal{U}_{|0\rangle}(\pi-\Delta\theta/2)\right] \approx U_{\rm BCH}$, with

$$\begin{aligned} U_{\rm BCH} &= \exp\left[-i\alpha'_j \boldsymbol{\sigma}\cdot(\hat{\mathbf{n}}_{1+}+\hat{\mathbf{n}}_{1-})\right] \\ &= \exp\left[i2\alpha'_j\boldsymbol{\sigma}\cdot\frac{-\hat{\mathbf{n}}_{1\perp}\sin\alpha_j\,\cos(\Delta\theta/2)}{\sin\alpha'_j}\right] \end{aligned} \quad [13]$$

where $\hat{\mathbf{n}}_{1\pm}$ are the *exact* effective vectors in the expressions for unitaries away from the sensing peak (Eq. 45),

$$\hat{\mathbf{n}}_{1+} = \frac{1}{\sin\alpha'_j}\left[\hat{\mathbf{n}}_{1\perp}\sin\alpha_j - \hat{\mathbf{n}}_0\sin(\Delta\theta/2)\,(1+\cos\alpha_j)\right]\cos(\Delta\theta/2)$$

$$\hat{\mathbf{n}}_{0+} = \frac{1}{\sin\alpha'_j}\left[\hat{\mathbf{n}}_{0\perp}\sin\alpha_j - \hat{\mathbf{n}}_1\sin(\Delta\theta/2)\,(1+\cos\alpha_j)\right]\cos(\Delta\theta/2)$$

For $N/2$ cycles of the CPMG experiment, this has the form

$$U_{\rm BCH}^{N/2} \approx \exp\left[iN\alpha'_j\cos(\Delta\theta/2)\frac{\sin\alpha_j}{\sin\alpha'_j}(\boldsymbol{\sigma}\cdot-\hat{\mathbf{n}}_{1_\perp})\right]. \quad [14]$$

Eq. (14) immediately reveals that the quantum interpolation compensation effect obtained when combining Eq. (6-7) in the interferometric signal cannot be captured by a simple BCH analysis. Indeed, while we expanded the fidelity in the small parameter $\Delta\theta$ in Eq. (11), $\Delta\theta$ is not a perturbative parameter in the BCH expansion, and in general the BCH expansion does not converge. If one were to use the first order BCH approximation, the compensation between the two propagators is lost and the flip angle is $\alpha'_j\cos(\Delta\theta/2)\frac{\sin\alpha_j}{\sin\alpha'_j}$, which only approaches the right expression when α'_j is small. Note however that we have made no assumptions in our analysis about α_j being small, and hence the simple zeroth order BCH analysis leads to a larger error than a more complete analysis that also includes the effect of commutators or cross terms.

1.5. Geometric representation of quantum interpolation.

While in the main paper we introduced a geometric picture of quantum interpolation as based only on a simple, visual intuition (Fig. 1.**A** of main text), here we provide more details of that representation, showing that it is indeed a faithful and quantitative representation of the unitary operators involved in quantum interpolation. We represent the unitaries obtained

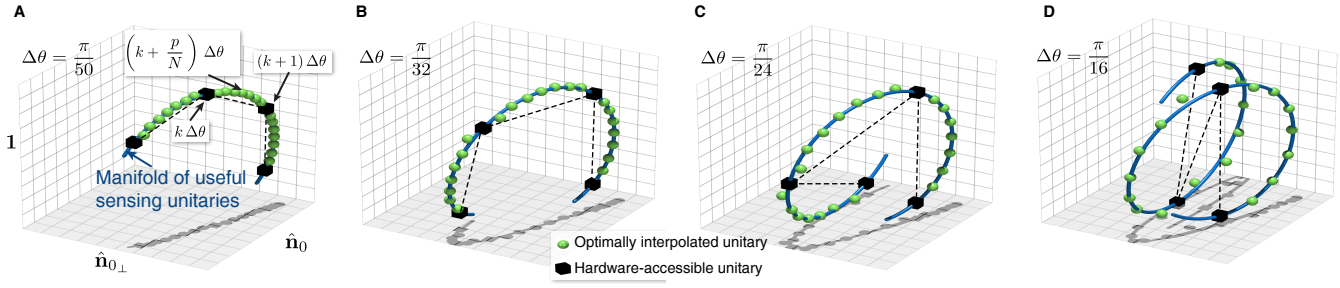

Fig. S5. Geometric picture of Quantum interpolation. We represent unitaries as points in the 3D space spanned by the operators $\{\mathbb{1}, \hat{\mathbf{n}}_0, \hat{\mathbf{n}}_{0_\perp}\}$. The projection of the missing dimension, $(\hat{\mathbf{n}}_0 \times \hat{\mathbf{n}}_{0_\perp})$ is small and only causes the norm of the vector to be smaller than one. The blue line indicates the ideal manifold of sensing unitaries, while the black squares represent the hardware accessible unitaries. Without quantum interpolation, the signal obtained by classical interpolation corresponds to the dashed black line. The green circles are the unitaries resulting from quantum interpolation following the optimal construction, where one seeks to construct the ideal unitaries $\mathcal{U}^N_{|0\rangle}(\pi - \delta_0 + k\Delta\theta)$, with $\delta_0 \in \{-\Delta\theta, 0, \Delta\theta, 2\Delta\theta\}$. Here $N = 8$ leading to 8 supersamples in each $\Delta\theta$ interval, and we set $\alpha_j = 0.1$ rad. The success of quantum interpolation is evident as the interpolated unitaries closely matches the target unitaries over the entire manifold, even for increasing values of $\Delta\theta$ (left to right panels).

from a quantum sensing experiment as vectors in 4D space [9]. As we consider only the *manifold* of the unitaries obtained by CPMG-like sequences as one sweeps through the sensing peak, we can reduce the space to 3 dimensions only (Fig. S5 and Fig. 1.**A** of the main paper). Indeed, from Eq. (67), the projection of the unitaries in the $(\hat{\mathbf{n}}_0 \times \hat{\mathbf{n}}_{0_\perp})$ dimension is small, and the unitaries can be represented to a very good approximation in the three dimensional space spanned by the vectors $\{\mathbb{1}, \hat{\mathbf{n}}_0, \hat{\mathbf{n}}_{0_\perp}\}$. Due to finite timing resolution one can only sweep this manifold in discrete steps (black squares in Fig. S5), but through quantum interpolation one can sample this manifold almost continuously (green circles). This is shown in Fig. S5 for increasing values of $\Delta\theta$ from left to right. In these simulations, we consider the construction of the ideal unitaries $\mathcal{U}^N_{|0\rangle}(\pi - \delta_0 + k\Delta\theta)$ via the optimal quantum interpolation construction, where δ_0 takes values $\delta_0 \in \{-\Delta\theta, 0, \Delta\theta, 2\Delta\theta\}$ about the sensing peak, and we considered $\alpha_j = 0.1$ rad and $N = 8$ CPMG cycles. It is evident that for small $\Delta\theta$ quantum interpolation accurately samples the exact manifold (blue line), while for increasing $\Delta\theta$ the approximation becomes slightly worse. It is remarkable that even with the rather large $\Delta\theta = \pi/16$ quantum interpolation very closely tracks the ideal manifold, a reflection of the second order error in Eq. (11).

2. Comparison with other high-resolution sensing techniques

Not only our quantum interpolation method compares favorably with other quantum sensing techniques, but in many cases it can be used to enhance these other techniques.

High-resolution magnetometry via NV-based sensing can be achieved with two other main approaches, besides XY8-based magnetometry, namely cross-polarization via resonant driving of the NV [10, 11] and correlation spectroscopy[12].

In the first technique, the NV center is spin-locked with a Rabi frequency Ω, and at the Hartmann-Hahn matching condition [13, 14] $\Omega = \omega_L + A_j$ there is a flow of polarization from the NV center to the resonant nuclear spin(s), which can be detected as a reduction in the NV polarization. Since this method does not rely on precise delays but instead on amplitude matching, the sensing resolution is set by the precision with which one can set the Rabi frequency. In practice, however, this technique is severely limited by amplifier noise that affects the stability of the spin lock, thus broadening the matching condition. Indeed, given typical amplifier noise

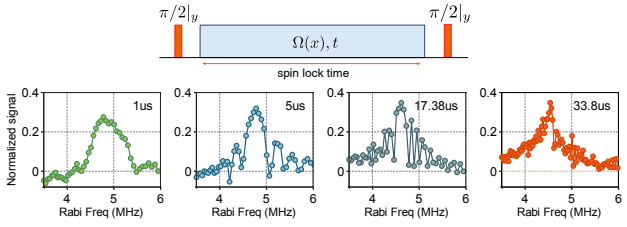

Fig. S6. Comparison with Hartmann-Hahn spin sensing. Here we vary the spin lock period at 1083G and study the sensing peak from a ^{14}N nuclear spin under the presence of a weak misaligned field (similar to Fig. 1.**B** of the main paper). The linewidth is Fourier limited by the spin lock period (shown in panels), and at long lock periods saturates due to amplifier noise. This is a representative example of the problem plaguing the ultimate achievable sensing resolution via the Hartmann-Hahn spin sensing technique.

of 8dB, corresponding to $T_{2\rho} \approx 40\mu$s for NV centers, the achievable resolution is only 25kHz. To demonstrate this, we performed Hartmann-Hahn experiments (Fig. S6) to sense a single ^{14}N nuclear spin in the presence of a static misalignment, giving rise to a signal similar to Fig. 1.**B** of the main paper. The sinc-like linewidth decreases linearly with the spin-lock time; however, the effect of amplifier noise is to relatively quickly saturate the linewidth and reduce signal contrast.

There have been proposals for overcoming amplifier noise, for instance by employing concatenated driving [15]. This relies on going into a doubly dressed basis that is immune to amplifier noise. However, it cannot easily be applied to high resolution sensing of nuclear spins because the modified Hartmann-Hahn condition now involves matching the Larmor frequency to the newly opened second order energy gap that is typically very small. This makes it difficult to match the Hartmann-Hahn condition selectively to few spins species, and hence obtain high resolution spectra. An alternative approach was proposed in Ref. [11]. Spin lock periods are interrupted by periods of free evolution under a gradient that creates an effective frequency filter, allowing potentially high resolution ≈200Hz. However, even this method is once again susceptible to finite timing resolution, for which quantum interpolation can be effectively employed.

A second important class of techniques is correlation spectroscopy [12]. The experiment consists of two blocks of XY8 sequences separated by a long delay t. The delay is swept and the target spin resonant frequency is obtained via Fourier transform. Since the delay t can be very long, $t \approx T_1$, one can achieve very high resolutions, for instance 470Hz in Ref. [16]. Unfortunately, the increased resolution comes at the cost of a great loss in sensitivity (contrast). Indeed for correlation spectroscopy the signal contrast goes $\propto \sin^2(N\alpha)$, where $N\alpha$ is the phase picked up by the NV during each XY8 interrogation period (Eq. 1 and S14 in [12]), while in XY8 sensing the contrast is $\propto \sin(2N\alpha)$ (assuming the same number of pulses). Thus, it is not possible to make a fair comparison of the two methods based only on frequency resolutions. Moreover, since XY8-sensing is a direct sampling technique as opposed to Fourier sampling in correlation spectroscopy, it is potentially more efficient for sampling sparse signal peaks and does not suffer from aliasing artifacts.

Still, since correlation spectroscopy experiments employ XY8/CPMG building blocks, quantum interpolation could be an important enabling tool in these experiments. More specifically, each XY8 building block should have time-delays that match the resonance frequency of the nuclear spins to be sensed, and is thus susceptible to finite-timing resolution. Quantum interpolation can be applied to mitigate this problem, translating into a potentially large boost in signal contrast (see Sec. 4.1). This enhanced resolution would also translate to a larger sensing bandwidth, allowing the resolution of spectral features without aliasing artifacts.

Finally, let us contrast our method with other proposals that also employ dynamical decoupling sequences with unequally spaced pulses. Ref. [17] employed 3 pulse blocks with unequal delays (variants of more general pulse families detailed in Figs. 7 and 8 in Ref. [18]) to resolve hidden spectral features. The sequence works by creating more filter function peaks (quantified by the parameter r in Fig. 2 of Ref. [17]), that however have much smaller amplitude. Indeed the

7/38 harmonic employed in [17] is over 10 times weaker than the primary filter harmonic, leading to a contrast loss in the resulting signal. Other r values have even poorer contrast (see Fig. 2 of Ref. [17]). Similar arguments can be made regarding sequences theoretically proposed in Ref.[19] (Fig. 2 of that paper). In contrast, quantum interpolation introduces *no* loss of signal contrast. The key advance in our work is a deterministic (and optimal) method to move the primary filter harmonic with a very fine step, and with an extremely small error. As a result, all the peaks are of the same amplitude up to second order in $\Delta\tau$. This can be ascribed to employing optimal interferences between spin propagators and is not merely a classical filter construction as considered in Refs. [17, 19]. Moreover since the construction is completely deterministic, one can sample only particular chosen samples of interest, a task that is not easily possible in previous proposals.

3. Optimal Quantum Interpolation Construction

The naive construction based on the approximation of Eq. (3) is not optimal, and carries the error that finally limits the number of additional supersamples that reliably constructed. Thus we develop an optimal construction for quantum interpolation to overcome this problem. The optimal construction sets the *order* of operators $\mathcal{U}(\tau_k)$ and $\mathcal{U}(\tau_{k+1})$ used to interpolate a supersample $q\Delta\tau/(p+q)$ with the lowest amount of error.

3.1. Error in sequence construction: Semiclassical analysis.

The simplest method to characterize the error of supersampling sequences is through a semiclassical analysis using the filter formalism of dynamical decoupling [20–23], as it enables a simple optical analogy [24]. Here we assume a classical noise field acting on the NV center, yielding the Hamiltonian $\mathcal{H}_n = bE_z(t)S_z$. Here $E_z(t)$ is a classical noise field, assumed to be Gaussian-distributed with zero mean. For instance, $E_z(t)$ might approximate the spin noise for an ensemble of weakly coupled nuclear spins. For stationary noise, the time-correlation is $\langle E_z(t)E_z(t+\tau)\rangle = g(\tau)$, with the noise spectral density $S(\omega) = \frac{1}{\sqrt{2\pi}}\int_{\infty}^{\infty} dt g(t)e^{-i\omega t}$. For example, the spectral density function due to nuclear spin noise is centered at their resonance frequency, with zero linewidth if considering a single nuclear spin. In the toggling frame, each π pulse in the control sequence flips the sign of the noise Hamiltonian $\mathcal{H}_n$, leading to the effective time-dependent Hamiltonian $\widetilde{\mathcal{H}} = bf(t)E_z(t)S_z$. The time-domain filter function $f(t)$ switches between ±1 at each pulse. The decay of the coherence of the NV center is then given by the overlap integral $\chi(t) = \frac{\sqrt{2\pi}|b|^2}{2}\int_{-\infty}^{\infty}|F(\omega)|^2 S(\omega)d\omega$, between the frequency domain filter $F(\omega)$ (the Fourier transform of $f(t)$) and the noise spectrum.

Now, given the finite timing resolution $\Delta\tau$, we can only obtained two different time-domain filter functions with total time separated by $4\Delta\tau$. The aim of quantum interpolation is to obtain a filter that leads to the same signal as the effective filter that is "in-between" these two hardware separated filters. While the error arises from differences between the ideal and interpolated $F(\omega)$, to evaluate the how closely this construction is a faithful representation of the ideal filter, by Parseval's theorem, one just needs to determine the deviation ϵ of the interpolated time-domain filter from the ideal one.

For the case of $U(\tau_k + \Delta\tau/2)$, the relative error is just $\Delta\tau/2\tau$, which is proportional to the size of the sampling interval. This provides a convenient starting point to determine the *optimal* interpolation construction for any arbitrary sampling point $\frac{q}{p+q}\Delta\tau$: Essentially the optimal construction is the one that minimizes the *net* deviation ϵ of the time-domain interpolated filter from the ideal one. Fig. S7 offers a simple prescription to calculate this error; the upper rail represents the filter corresponding to the quantum interpolation construction out of $\mathcal{U}(\tau_k)$ and $\mathcal{U}(\tau_{k+1})$ operators, while the lower rail represents the ideal filter. The total length for both rails is identical – this ensures that the filter does indeed sample the correct frequency. Comparing each filters for each successive application of operators (i.e. piecewise), one obtains trapezium shaped blocks that can be pieced together to evaluate the error of a supersampling sequence. The net error of each of these blocks has the form (see Fig. S7),

$$\epsilon = \left|-\frac{3}{4}\Delta a + \frac{1}{4}\Delta b\right| + \left|-\frac{1}{4}\Delta a + \frac{3}{4}\Delta b\right| \qquad [15]$$

The optimal constructions, for instance shown in the lower panels of Fig. S7 for $U(\tau+\Delta\tau/2)$ and $U(\tau+\Delta\tau/4)$ minimize this error. Note that the error in Eq. (15) is maximized in the situation where Δa is negative, and Δb positive, giving the bound,

$$\epsilon \leq (\Delta a + \Delta b) \qquad [16]$$

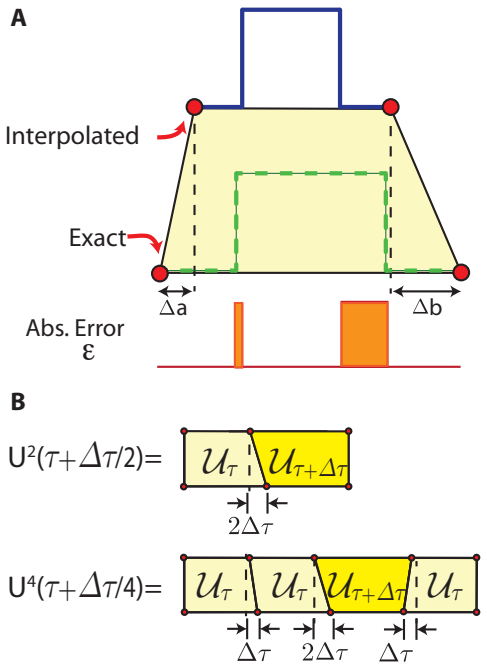

Fig. S7. Evaluating construction error via the filter formalism. (A) Here the upper rail of the trapezium represents the interpolated construction (approximate), and the lower rail represents the target construction (ideal) (see also Fig. S9). The circles denote the *total* period of the corresponding interpolated (blue line) and exact time domain filter functions (green dashed lines), corresponding to Fig. 1.**C** of the main paper. Δa and Δb denote the deviations of the interpolated filter from the exact one, and the net error is then $\epsilon = \left|-\frac{3}{4}\Delta a + \frac{1}{4}\Delta b\right| + \left|-\frac{1}{4}\Delta a + \frac{3}{4}\Delta b\right|$, which is minimized by the optimal supersampling construction. **(B)** Optimal constructions for the quantum interpolated points one-half and one-quarter between two hardware defined samples (see also Fig. S10).

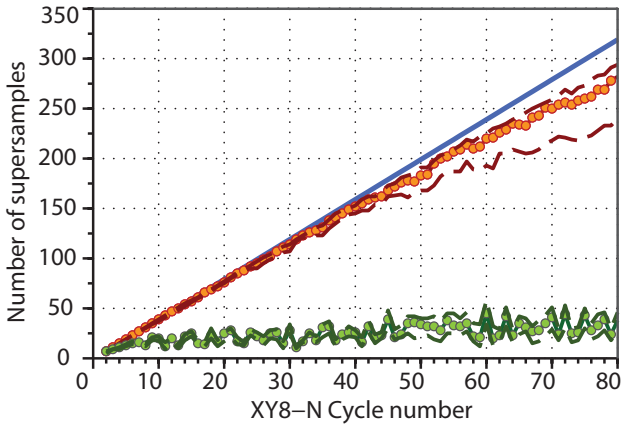

Fig. S8. Gains in resolution via supersampling. Here we consider $\alpha_j = 0.1$ rad and $\Delta\theta = \pi/20$, which for conventional magnetic fields used for spin sensing corresponds to a timing resolution $\Delta\tau$ of a few nanoseconds (typical for hardware). We consider the scaling of the number of supersamples possible via quantum interpolation constructions for XY8-N sequences. The maximum number of samples (blue line) grows linearly with N. The green line quantifies the samples obtained via the construction of Eq. (3), where the points indicate a fidelity better than 0.9 over a range of $\delta \in [-\Delta\theta/2, \Delta\theta/2]$, while the dashed lines indicates fidelity >0.85 (upper dashed line) and >0.95 (lower dashed line). As is evident, the number of samples grows $\propto N$ for small N, before saturating. The optimized construction obtained in Sec. 3 is shown in the red points. Decreasing $\Delta\theta$ further (see Fig. S5) will lead to an even larger number of supersamples before saturation. The numerical results indicate that one can reliably achieve resolution gains by over three orders of magnitude using quantum interpolation.

3.2. Analysis via quantum mechanical propagators. While in the previous section we derived the optimal construction based on a semiclassical (filter) analysis, here we show that the optimal construction is also a faithful approximation of the desired evolution for the *quantum* systems that the quantum sensor is probing.

Specifically, we consider the infidelity of quantum interpolation operators with respect to the the ideal propagator and perform a numerical analysis of the infidelity of *every* permutation, for a broad range of values of δ_0 (the deviation from sensing peak in angle unit) close to the sensing peak. In general, we find that the plot is qualitatively similar for different values of $\Delta\theta$, the range of δ_0, and the value of α_j.

3.3. Scaling of number of supersamples. Let us now characterize the theoretical number of supersamples one can achieve via quantum interpolation, and the effective boost in sensing resolution. From the geometric construction of the algorithm in Fig. S9, it is evident that for N cycles of the CPMG sequence, one has a set of N points on the right half circle, and hence one can obtain a total N supersamples in every $\Delta\tau$ interval.

However, given an maximum error bound, the number of supersamples will at some point deviate from this linear scaling. To study this in detail, we performed numerical simulations (see Fig. S8) considering a spin with $\alpha_j = 0.1$ rad and $\Delta\theta = \pi/20$ (as for typical hardware), and considered the number of supersamples that have a fidelity better than 0.9 (points), 0.95 and 0.85 (dashed lines) over a range of $\delta \in [-\Delta\theta/2, \Delta\theta/2]$. The fidelity was calculated by evaluating the overlap of the interpolated unitary with the ideal one, similar to Eq. (11). In Fig. S8, the blue line shows the theoretical maximum number of supersamples grows linearly with N, while via the optimal construction one can achieve a linear scaling upto $N = 200$ (green points), allowing for an effective increase in resolution by over two orders of magnitude. Decreasing $\Delta\theta$ further will increase the range over which the scaling of supersamples is linear. Note that the naive construction (Eq. 3) also has a linear scaling for small N, but it quickly saturates after $N > 15$ due to the accumulation of error, pointing out again the need for the optimal construction.

Ultimately then, through the optimal quantum interpolation construction, the resolution achievable can be made largely dependent only on the number of pulses that can be reliably applied to the system. The linear scaling of the number of samples can exactly and completely mitigate the deleterious effects of finite resolution.

3.4. Algorithm for optimal supersampling construction. Let us now determine the supersampling construction that minimizes the error ϵ in Eq. (15) – the deviation from the ideal filter. For a sample of the form sample $= q/(p+q)$, we obtain the optimal string of operators $\mathcal{U}(\tau_k)$ or $\mathcal{U}(\tau_{k+1})$ with the minimization evaluated at the end of each applied operator following Fig. S7. We note that while in principle one has to minimize the deviation of the time domain filters edge to edge in Fig. S7, however it is sufficient to use a simple approach of minimizing deviations in the total periods. A simple algorithm that achieves this has the pseudocode in Fig. S11. The optimal construction is shown in Fig. S10, where the colors represent the operators $\mathcal{U}(\tau_k)$ or $\mathcal{U}(\tau_{k+1})$. The panels describe the construction of different supersamples, the total number of which scales linearly with the number of pulses (shown are the examples of XY8-4 and XY8-8). See Fig. S20 for the actual full algorithm of generating optimal quantum interpolation sequence.

A geometric interpretation of this algorithm, similar to Householder rotations [9, 25] is described in Fig. S9. The

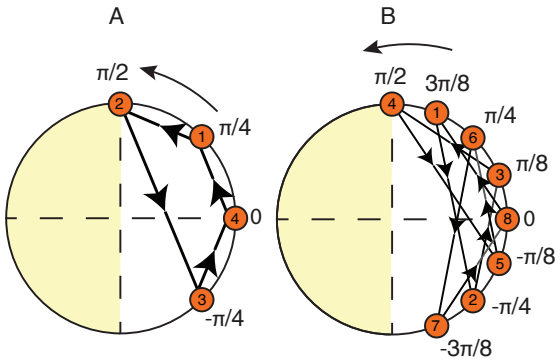

Fig. S9. Geometric representation of the optimal construction, for two particular sampling times **(A)** $\Delta\tau/4$ and **(B)** $3\Delta\tau/8$. We represent the desired sample as phasor at angle $\pi \times$ sample on a circle (orange circles). The left half plane (LHP) of the circle (shaded) is considered forbidden. Starting with an initial loop counter $m = 0$, we propagate the algorithm by forming the phasor $m \to m +$ sample (arrows); and so long as we don't pass into the LHP we assign to this the operator $\mathcal{U}(\tau_k)$. In the opposite case, we assign $\mathcal{U}(\tau_{k+1})$, and reflect the phasor about the origin. The algorithm ends when we finally return to the starting position. The numbers in the orange circles indicate the progression of the algorithm. This geometric representation also allows an intuitive understanding of why the error of all samples is almost the same (see Fig. S12).

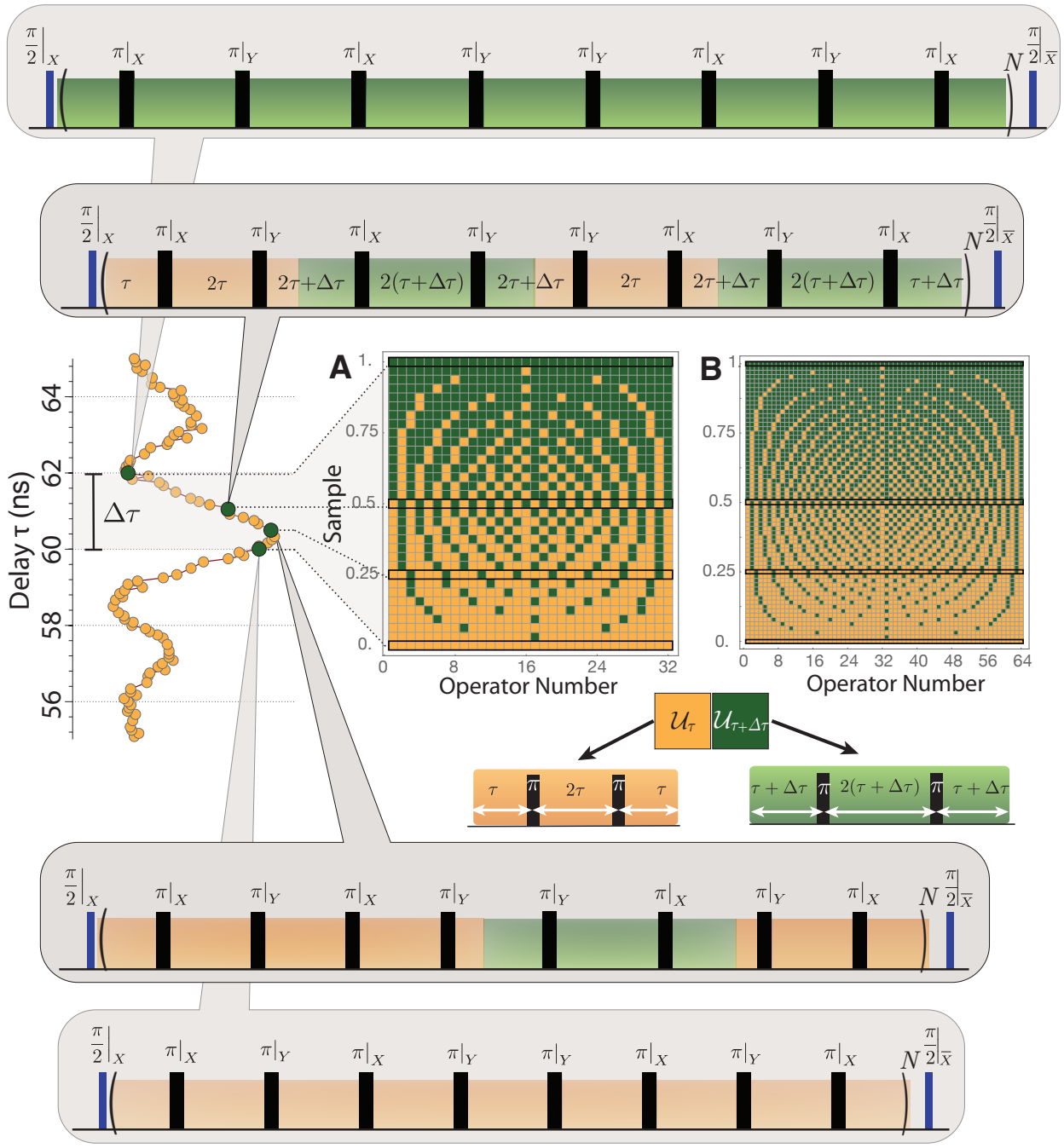

Fig. S10. Pulse sequence construction for optimal quantum interpolation. Shown is the optimal quantum interpolation supersampling construction for different samples for **(A)** N=8 and **(B)** N=16 cycles of an XY8 sensing sequence. Here "sample" refers to point to be interpolated between two hardware limited intervals as the fraction of the timing resolution $\Delta\tau$. For reference example experimental data is shown (red circles, corresponding to Fig. 1.**B** of the main paper). Here $\Delta\tau = 2$ns, and in each such interval one could effective supersample proportional to the number of pulses applied. To experimentally construct the optimal interpolated sequence for a sample corresponding a particular row of the matrix, one applies the sequence of operators $\mathcal{U}(\tau_k)$ (white) or $\mathcal{U}(\tau_{k+1})$ (red) from left to right. The boxed inset panels denote the pulse sequences corresponding to four example samples – $\{0, 1/4, 1/2, 1\}$.

Algorithm 1 : Construction of the optimal interpolation sequence

procedure OPTIMALCONSTRUCTION
  Set loop iteration counter $m \leftarrow 0$
  Optimal sequence string $U \leftarrow$ null
  loop:
  Propagate $m \leftarrow m +$ sample
  if $|m| \leq 1/2$ **then** Append $\mathcal{U}(\tau_k)$ operator to sequence
  else
    Append $\mathcal{U}(\tau_{k+1})$ operator to sequence
    Reflect $m \leftarrow m - 1$
  while $m \neq 0$ **do**
    goto ***loop***
  end procedure

Fig. S11. Algorithm for optimal quantum interpolation construction. The algorithm produces the optimal sequence of $\mathcal{U}(\tau_k)$ and $\mathcal{U}(\tau_{k+1})$ operators to interpolate the desired sampling point. In the algorithm, "sample" stands for a fraction between 0 and 1 corresponding to the desired supersample time.

required sample can be represented as a phasor on a circle, at an angle $\pi \times$ (sample). The algorithm is composed of two steps – *propagate*, or *propagate and reflect*, associated with the application $\mathcal{U}(\tau_k)$ or $\mathcal{U}(\tau_{k+1})$ operators respectively. Geometrically, one keeps propagating along points on the circle that differ by the required sample, and reflect every time when one trespasses into the left half circle (shaded region in Fig. S9). The algorithm ends when the phasor returns to the starting point. It is evident then for a sample $\Delta\tau/N$, one needs N operators in the construction.

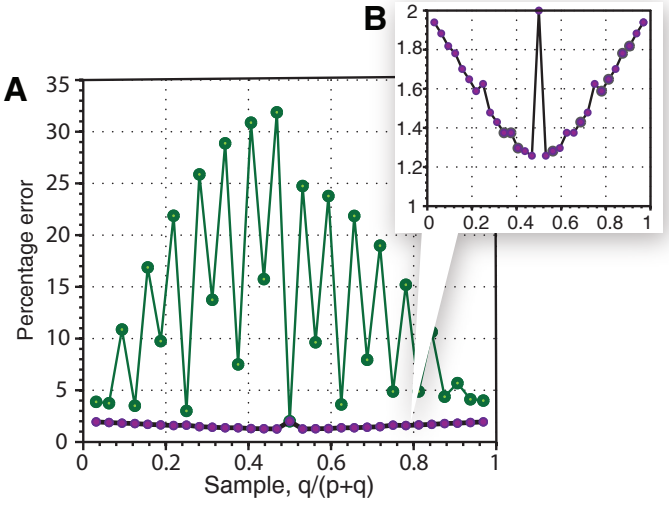

Fig. S12. Performance of optimal quantum interpolation. We represent the percentage errors (specified in units of $\Delta\tau/4\tau$) of the construction of a supersample $[q/(p+q)]\,\Delta\tau$ via quantum interpolation using two hardware defined unitaries $\mathcal{U}(\tau_k)$ and $\mathcal{U}(\tau_{k+1})$, and an time resolution of $\Delta\tau$. Here we consider $N = 16$ cycles of the CPMG sensing sequence, giving a total of 32 possible supersamples. The error is calculated from the effective area under the time domain error function ϵ following Fig. S7. **(A)** The green points denote the naive construction $\mathcal{U}(\tau_k)^p\mathcal{U}(\tau_{k+1})^q$, where the errors accumulate very quickly. The purple line and points instead denote the case of the optimal construction following Fig. S9, where the error of all samples is less than the half-way-sample (zoomed in the inset **(B)**). Hence the optimal construction can reliably produce different supersamples with low effective error (see also Fig. S13).

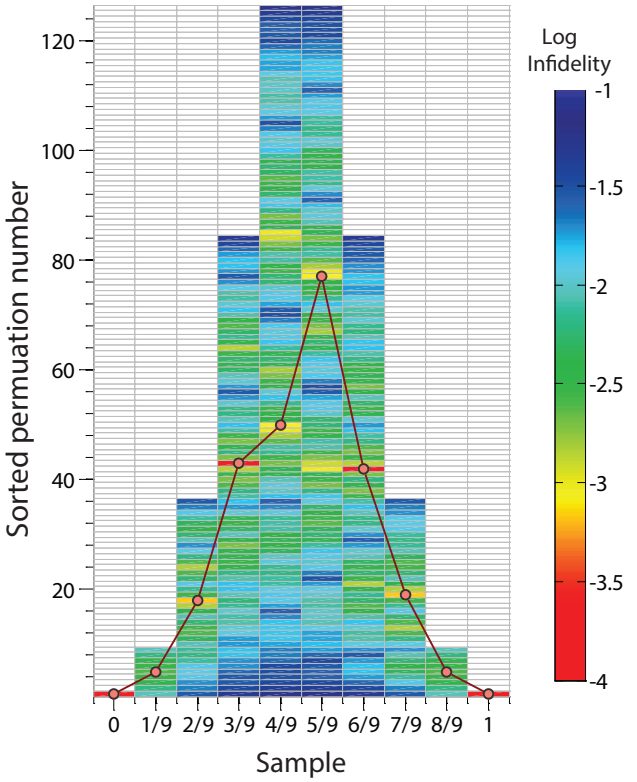

Fig. S13. Evaluating optimality of quantum interpolation constructions. Figure evaluates the optimal quantum interpolation construction for $N = 9$ cycles of the CPMG sequence. For every sample, of the form $p\Delta\tau/N$, for integral p, we evaluate the fidelity of the interpolated unitary obtained from hardware defined unitaries $\mathcal{U}(\tau_k)$ and $\mathcal{U}(\tau_{k+1})$ to the target unitary, for *every* possible permutation of $\mathcal{U}(\tau_k)$ and $\mathcal{U}(\tau_{k+1})$. For clarity, for instance, for the sample 1/9, there are 8 permutations of the sequence $[\mathcal{U}(\tau_k)\mathcal{U}(\tau_{k+1})^8]$, and we study the infidelity of each of these permutations (second bar). Here we evaluated the mean infidelity over the range $\delta_0 \in [-2\Delta\theta, 2\Delta\theta]$, for $\Delta\theta = \pi/20$ and $\alpha_j = 0.1$ rad. The permutations are sorted down to up by Hamming weight, i.e. in increasing decimal order of their sequence strings. The colors represent the log of the infidelity, and the smaller number represents that the constructed unitary is better, i.e. has lower error. The optimal construction obtained using the Algorithm in Fig. S11 are shown in the by the orange circles. Numerically, we find that the construction from Fig. S11 does indeed capture the optimal possible permutation.

As the optimal construction compensate the error at each step, it is significantly better than the naive construction $\mathcal{U}(\tau_k)^p\mathcal{U}(\tau_{k+1})^q$ that lets the error accumulate (see Fig. S12). Consequently, the number of supersamples achievable via quantum interpolation scale linearly with the number of pulses to a large extent (Fig. S8). More interestingly, this also implies that the error of all supersamples is approximately the same and bounded by the error of the $\mathcal{U}(\tau_k + \Delta\tau/2)$ as we shall show below.

3.5. Error of the Optimal Quantum Interpolation Construction.

While in principle we expect that each quantum interpolation construction, achieving supersampling at a different sampling point, might have a different error, here we show that for the same number of pulses, the error is always bounded by the error of $\mathcal{U}(\tau_k + \Delta\tau/2)^N$ (see inset of Fig. S12). For clarity, let us first consider the simple case when $N = 2^k$ and calculate the error of any of the supersamples. From the geometric

picture in Fig. S9, all samples of the form $\ell\Delta\tau/2^k$ for integral (ℓ, k) traverse the *same* set of points on the right half circle. Since Δa and Δb are now constrained to be points on the right half circle in Fig. S9 the net error can be calculated from Eq. (16) to be

$$\begin{aligned}\epsilon &\leq 2\Delta\tau \times 2(\text{sum of all points on right half circle}) \\ &= 2\Delta\tau \times 2\left(2\sum_{\ell=0}^{2^{(k-1)}-1}\frac{\ell}{2^k}+\frac{1}{2}\right) = 2^k(2\Delta\tau), \qquad [17]\end{aligned}$$

Hence the net error is bounded by $\epsilon \leq 2^{k-1}(4\Delta\tau)$, exactly the error of $\mathcal{U}_{1/2}^{2^k}$, which is the construction of the half-way-sample with the same number of pulses. An analogous calculation and graphical approach can be made for general N, and once again it is easy to show that that the error of all supersamples is bounded by that of $\mathcal{U}(\tau_k + \Delta\tau/2)$. This is convenient because it allows a simplification of the error analysis of supersampling, which is bounded by the analytical results obtained in Sec. 1.2, where we evaluated the error of $\mathcal{U}(\tau_k + \Delta\tau/2)$ and quantified its dependence on the size of the sampling interval $\Delta\tau$.

4. Advantages of Quantum Interpolation

4.1. Deleterious effects of finite sampling.

4.1.1. Loss in sensing contrast. Often we are interested in resolving spins that are very close together in frequency, for instance to be able to reconstruct their positions and the structure of the spin network of which they are part. The differences in frequency arising for instance from chemical shifts could be as small as $10^{-6}\omega_L$. In a real experimental scenario however, the rotations on the nuclear spins via the NV are effectively achieved through delayed evolution as in Fig. S16, and the construction of Eq. (48) is prone to finite-sampling effects, leading to a loss of signal contrast and resolution. In this section, we quantify these deleterious effects in detail.

Consider for interferometric spin sensing, we would like ideally to construct the CPMG sequence by matching the delay $2\tau = \pi/\omega_L$; however given a finite sampling resolution $\Delta\tau$, one has a finite error that directly translate to a deviation from the ideal signal peak. For instance in Eq. (36), this translates to errors in the rotation flip angles of $\pi/2$ and π that constitute a perfect CPMG spin sensing sequence – instead, these angles can now only be achieved to within the sampling interval $\Delta\theta = \omega_L\Delta\tau$ (see Fig. S1).

In the following, we shall quantify the deleterious effects of the this finite timing resolution:

1. Due to the fact that the signal linewidth decreases with the number of cycles N, finite sampling resolution $\Delta\theta$ might cause the sensing peak to be *lost* beyond a threshold) $N_{\max}$. This is experimentally demonstrated for instance in the left panels of Fig. 1.**B** of the main paper, where the sensing peak is just a single point or less and is not efficiently sampled.

2. For a deviation away δ_0 from the perfect interferometric construction, we will show below that the signal falls away quadratically with δ_0 and the number of cycles N. This leads, very quickly, to the underestimation of the sensing peak contrast, that can lead to significant error in reconstructing the hyperfine term B_j for spin sensing experiments.

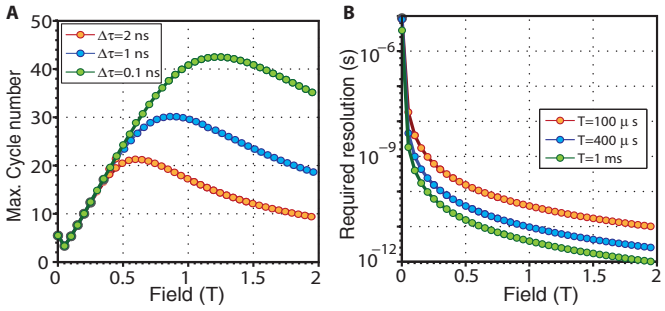

Fig. S14. Effects of finite timing resolution. (A) Panel denotes the maximum number of CPMG cycles N before one becomes sensitive to finite timing resolution effects. Here we consider a single ^{1}H spin that is 2.45nm away from the NV center at relative coordinates [1,1,2]nm to the NV center. As is evident, at moderately high magnetic fields > 0.5T, one quickly becomes prone to subsampling effects. **(B)** Panel denotes the largest $\Delta\tau$ required to still be not prone to subsampling effects, i.e. the largest $\Delta\tau$ required to still efficiently sample the signal peak. We consider here different total times of the sequence, limited by the maximum $T_2 \approx 1$ms. Even for moderately high magnetic fields, one requires a timing resolution of a few picoseconds, which is at the limit of current hardware. Quantum interpolation based supersampling allows us to achieve a small effective $\Delta\tau$ from modest available hardware.

3. Finite resolution also leads to a decrease in the maximum achievable peak signal, directly affecting the *sensitivity* of the NV based spin sensor.

Let us first evaluate the maximum number of cycles $N_{\max}$ such that the linewidth $w/\omega_L \leq \Delta\theta$, i.e. after which we become susceptible to finite sampling effects. From Eq. (49),

$$N_{\max} \approx \frac{\pi}{\sqrt{(\omega_L\Delta\tau)^2(1+\cos\alpha_j)^2+\sin^2\alpha_j}} \qquad [18]$$

For instance for a hardware set timing limitation of $\Delta\tau$=1ns (see Fig. S14(**A**)), for a weakly coupled ^{1}H spin at 0.5T and $\alpha_j = 0.05$rad, we have that the maximum XY8-N experiment that can be applied is $N_{\max} \approx 12$. This is a very small number of cycles, and increasing N beyond $N_{\max}$ leads to subsampling of the peak signal, leading to a substantial loss of contrast.

Let us now in determine in detail the loss in signal contrast and resolution. Let us define sampling error $\delta_0 = \pi - k\Delta\theta$ where k is integral (Fig. S1), and which denotes the deviation from the perfect CPMG sensing sequence (the perfect sequence in Eq. (36) refers to $\delta_0 = 0$). The signal contrast $C(\delta_0) = \frac{1}{2}[1 - S(\delta_0)]$ is now,

$$C(\delta_0) = \frac{1}{2}\sin^2(N\alpha_j')\,(1-\cos\alpha_j') + \frac{\sin^2(N\alpha_j')}{\sin^2\alpha_j'}\sin^2\alpha_j\cos\alpha_j \qquad [19]$$

while the perfect contrast $C(0) = \sin^2(N\alpha_j)[1+\cos(\alpha_j)]$. For small sampling error δ_0, one can now evaluate the effective loss in contrast,

$$\epsilon = C(0) - C(\delta_0) = \frac{1}{4}(N\alpha_j)^2\delta_0^2\left(2-\frac{\alpha_j^2}{2}\right)^2 \qquad [20]$$

This expression is good upto second order in δ_0, and captures the scaling of the contrast loss $\epsilon \propto N^2\delta_0^2$, i.e. as the number of cycles N increases or as one improperly samples the signal peak (larger $\Delta\tau$), the loss in contrast increases quadratically. This is also evident in the experimental data shown in the left panels of Fig. 1.**B** of the main paper – the sensing peak is

improperly sampled, and the structure in the peaks cannot be resolved.

While Eq. (20) considered the loss in contrast for small δ_0, let us consider now the maximum bound on the contrast $C_j(\delta_0)$. We will show that the signal not only grows quadratically slowly following Eq. (20), but is also upper bounded to a significantly lower level. Consider that maximum contrast at the peak $C(0)|_{\max} = 1 + \cos\alpha_j$, while at finite δ_0 we have,

$$C(\delta_0)|_{\max} = 1 + \frac{\cos(\alpha_j)\left[\sin^2(\alpha_j) - \delta_0^2(1+\cos\alpha_j)^2\right]}{\sin^2(\alpha_j) + \delta_0^2(1+\cos\alpha_j)^2} \quad [21]$$

It is quite easy to see that $C(\delta_0)|_{\max} < C(0)|_{\max}$. For instance, for $\delta_0 \gg \sin\alpha_j$ (meaning one is away from the sensing peak), we have $C(\delta_0)|_{\max} = 1 - \cos(\alpha_j) \to 0$ since α_j by definition is small. This quantifies the intuition of destructive interference affecting the flip angle α_j into α_j' (see Eq. (46)) as one moves away from the sensing peak. In contrast in the perfect case $C(0)|_{\max} = \frac{1}{2}(1+\cos\alpha_j) \to 1$. Hence, in summary, one can quantify the deleterious effects of limited timing resolution $\Delta\tau$ with regards to signal contrast: not only does the signal grow quadratically slower with N and δ_0, but it is also upper bounded to a lower level.

4.1.2. Loss in sensing resolution. In addition to a loss of signal contrast, in this section we show that finite timing resolution $\Delta\tau$ also leads to a loss of sensing *resolution*. Consider that the effective linewidth in time units (Eq. 49) is given by $\Delta\tau_{\rm lw} = w/\omega_L = \frac{[\sin^2(\pi/N)-\sin^2(\alpha_j)]^{1/2}}{2\omega_L\cos(\alpha_j/2)}$, however the hardware limits us to effectively a resolution of $\Delta\tau$. In order to resolve the signal peak faithfully we have the requirement that $\Delta\tau \leq \frac{1}{2}\tau_{\rm lw}$. Along with the fact that the number of pulses is bounded by the coherence time, $N_{\max} = \frac{T_2\omega_L}{2\pi}$, this translates to

$$\Delta\tau \lesssim \frac{1}{2\sqrt{2}\omega_L\cos(\alpha_j/2)}\sin\left(\frac{2\pi^2}{T_2\omega_L}\right) \quad [22]$$

Eq. 22 quantifies the fact that one needs a better timing resolution (smaller $\Delta\tau$) as one goes to higher magnetic fields, or higher number of cycles. For instance (see Fig. S14**(B)**), for a ^{1}H nuclear spin at a field of 0.5T, assuming $T_2 = 1$ms and $\alpha_j = 0.05$rad typical for a weakly coupled spin, Eq. (22) sets the requirement $\Delta\tau \leq 15.83$ps, which is a very small required timing resolution. If $\Delta\tau$ does not satisfy Eq. (22), then the sensing peak can be completely lost. This is demonstrated also in the left panels of Fig. 1.**B** of the main paper, where poor sampling resolution does not allow us to resolve the structure in the ^{14}N signal (that follows Eq. (48)).

4.2. Gains in resolution: Q-value of quantum interpolation.

In order to characterize the boost in resolution granted by supersampling, we introduce as figure of merit the Q-value of the sensing peak, $Q = f_{\rm AC}/\Delta f_{\rm AC}$. Given that the sensing peak arises at time $\tau = 1/f_{\rm AC}$, and the sensing linewidth in time units is w, we have the frequency linewdith

$$\Delta f = \frac{1}{\tau - w} - \frac{1}{\tau + w} \approx \frac{2w}{\tau^2} = 2wf_{\rm AC}^2 \quad [23]$$

giving $Q \approx 1/[2wf_{\rm AC}]$. This definition of Q describes the ability to resolve sensing peaks at different frequencies, where the minimum condition to resolve two sensing peaks is that the peaks are separated by at least $2w$. The Q-value scales linearly

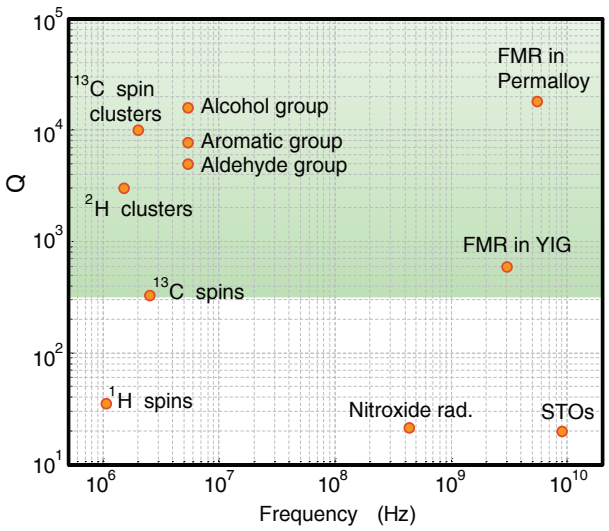

Fig. S15. Q-value vs f for different quantum metrology experiments. In this scatter plot we show representative examples the Q-values from different signal sources plotted against their native frequency f (see Table S1). Note that in our experiments, we could obtains gains in Q by about 10^4 via quantum interpolation, and this might open up the metrology of several signals (green shaded region) that were hitherto extremely challenging.

with the number of pulses N, since ideally $w \propto 1/N$. However, in practice w is bounded by the finite timing resolution $\Delta\tau$. Let us now evaluate the maximum achievable Q-value in this situation of limited $\Delta\tau$. Then, the smallest linewidth one can achieve for sensing is $w = \Delta\tau$, giving the bare Q-value

$$Q_{\rm bare} = \frac{1}{f_{\rm AC}(2\Delta\tau)}. \quad [24]$$

Quantum interpolation can boost the Q-value by overcoming the limits in sampling time, $\Delta\tau$. This is shown for instance in Fig. 2 of the main paper, where $\Delta\tau = 1$ns restricts $Q_{\rm bare}$ to a maximum of 100. Thanks to quantum interpolation, where the number of possible supersamples scales linearly with the pulse number, the Q-value is limited in principle only by the intrinsic linewidth of the sensing peak, given by the total time of the experiment. At the maximum allowed time, that is $T = T_2 \approx 1$ms, we can estimate the Q-value under quantum interpolation using Eq. (50),

$$Q_{\rm supersample} = \frac{\sqrt{2}\cos(\alpha_j/2)}{\sin\left(\frac{2\pi^2}{T_2\omega_L}\right)}. \quad [25]$$

Hence, due to quantum interpolation, one achieves a boost in the sensing Q value by an amount,

$$Q_{\rm boost} = \frac{Q_{\rm supersample}}{Q_{\rm bare}} = \frac{\Delta\tau}{w} = \frac{\sqrt{2}\Delta\tau\omega_L\cos(\alpha_j/2)}{\sin\left(\frac{2\pi^2}{T_2\omega_L}\right)} \quad [26]$$

where we have used the expression in Eq. (22). Figure 2.**D** of the main paper, obtained from the experiments in Fig. 2.**C**, illustrates that the effective sensing $Q = f/\Delta f$ can be boosted by a factor of 1000. However this experiment was performed with a total time of 115.2μs. At the T_2 of 330μs experimentally demonstrated for shallow NV centers in [26], $Q \approx 2893$. Given the rapid improvements in coherence times over the past few years, it is reasonable to expect that $T_2 \approx 1$ms is achievable for shallow NVs in the near future (it is already routine for

Experiment/system	Signal source	f	Δf	Q-value	Reference	Notes
Nanoscale NMR/ESR	^{13}C spins	2.5 MHz	7.5 kHz	333	[26]	Nanoscale spin sensing experiments on a single protein of Ubiquitin.
	Nitroxide rad.	430 MHz	20 MHz	21.5	[28]	Electron radicals measured in a single protein.
	^{1}H spins	1.06 MHz	30 kHz	35.3	[29]	Proton spins measured in an organic molecule outside diamond.
	^{13}C spin clusters	2 MHz	200 Hz	10^4	[11]	Simulated linewidth required to resolve clusters of spins in CXCR4.
	Nanoscale NQR of ^{2}H clusters	1.5 MHz	500 Hz	3000	[26]	Simulated linewidth required to resolve NQR peaks arising in deuterated phenylalanine.
^{13}C chemical shift	Aldehyde group	5.35MHz @ 0.5T	-	$\sim$ 5000	[30]	We assume that to be able to resolve chemical shifts, one requires a Q of at least the shift value.
	Aromatic group			$\sim$ 7700		
	Alcohol group			$\sim$ 16000		
Spin waves in Ferromagnets	FMR in Permalloy	5.5 GHz	0.3 MHz	1.8×10^4	[31]	Here we consider *spectrally* sensing the spin waves excitations directly via the NV.
	FMR in YIG	3 GHz	5 MHz	600	[31, 32]	
	STOs	9 GHz	450 MHz	20	[33]	Spin torque switching in Tantalum.

Table S1. Examples of Q-values from different sources. In this table we show representative examples of Q-values required to effectively sense signals from different sources, including single spins, chemical shifts, and spin wave modes in ferromagnets (see also Fig. S15). We note that most measurements in the literature are of low Q-value, below 1000. Given that we can experimentally achieve substantial gains in Q-value due to quantum interpolation, several of the high Q signals are now within the regime of quantum metrology with NV centers.

bulk NVs [27]). This would allow one to approach a Q-value of 10^4 that, along with quantum interpolation, could allow NV based sensors to measure fields with high resolution from varied sources.

4.3. Applications to quantum metrology experiments. The Q-value provides a convenient measure to characterize the gains due to quantum interpolation. In our experiments, we were able to achieve substantial gains in Q-value over the bare limit set by the hardware. More broadly, quantum interpolation is useful for NV-based sensing of signals that have high Q, for instance, signals with extremely small Δf (narrow linewidths or frequency differences) such as nuclear spins and chemical shifts, or signals with high frequency f, such as spin wave modes in ferromagnets. Many of these signals are currently out of reach because of the severe constraint set by timing resolution. In the case of high frequency signals (for instance FMR in ferromagnets), we envision sensing higher harmonic of the signal for which the time τ is greater than the pulse width. Then, thanks to quantum interpolation the time can be swept with a very fine step, allowing one to detect high-Q, high f signals. Quantum interpolation would then significantly broaden the impact of NV center as a probe for condensed matter systems, as we show in detail Table S1 and Fig. S15, where the Q-values are plotted against frequency.

5. Experimental setup

Nitrogen-vacancy (NV) centers in diamond are substitutional nitrogen atom close to a vacancy in the carbon lattice [34]. Their electronic spins possess remarkable quantum properties that persist at room temperature. The spin state of the negatively charged NV center has an exceptionally long coherence time and its electronic level structure allows efficient, all-optical spin polarization. The NV can be optically excited by a 532 nm laser light and it emits at 637 nm. It has a zero-field splitting of 2.87 GHz between the $m_s = |0\rangle$ and $m_s = |\pm 1\rangle$ states. A magnetic field splits the $m_s = |\pm 1\rangle$ levels allowing selective microwave excitation of the spin transition.

In the experiment we used NV centers that are created in an optical grade, isotopically pure diamond (99.99% C-12, purchased from E6) via implantation and subsequent annealing. Single NV centers are addressed using a home-built confocal microscope. In the microscope, a collimated 532 nm laser (SPROUT from Lighthouse Photonics) beam is first sent through an acousto-optic modulator (AOM, Isomet Corporation, M113-aQ80L-H) for switching and then focused using an oil immersion objective (Thorlabs N100X- PFO Nikon Plan Flour 1.3NA). The sample is mounted on a 3D-piezo scanner (Npoint) to position at the microscope focus with nm precision. The fluorescence excitation light is collected by the same objective, collimated, filtered from the 532 nm beam using a dichroic (Chroma NC338988) and then focused onto a pinhole for spatial filtering. The NV center fluorescence was filtered with a 532 nm notch filter (Semrock, BLP01-594R-25) and a 594 nm long-pass filter (Semrock, BLP01-594R-25) and collected using a single-photon counting module (Perkin Elmer SPCM-AQRH-14).

In our experiments, we generate microwave pulses to construct quantum interpolation dynamical decoupling sequences using the following hardware:

1. Direct synthesis of the pulses using 1.25 GS/s four channel arbitrary waveform generator(Model WX1284C, Tabor Electronics Ltd.). This has a timing resolution of $\Delta\tau =$ 1ns, and is employed in experiments described in Fig. 2 of the main paper.

2. By using a microwave signal generator (Stanford Research Systems SRS 384) gated by a 500 MHz PulseBlasterESR-PRO pulse generatorfrom Spincore Technologies through a microwave switch (Minicircuits ZASWA-50-DR+). The PulseBlaster has a timing resolution of $\Delta\tau = 2$ns, and this is employed in experiments described in Fig. 1 and Fig. 3 of the main paper.

The MW pulses are subsequently amplified using a high power amplifier (Minicircuits LZY22+). The AWG, the AOM and the single-photon counting module were gated using TTL pulses produced by the 500 MHz PulseBlaster. The static magnetic field is generated using a 1T surface magnetization permanent magnet (BX0X0X0-N52) obtained from K&J Magnetics. The magnet assembly is mounted on a combination of motorized

translation and rotation stages (Zaber TLA series) that are used to align the field to the [111] axis of the NV center.

6. Interferometric spin sensing via the NV center

Although the principle of nuclear spin sensing by NV centers has been discussed extensively, the method is very often presented with a semi-classical picture of the nuclear spin noise and the filter formalism. For a better understanding of quantum interpolation, we need instead to more precisely evaluate this interferometric method by considering the full quantum mechanical evolution of the the nuclear spins [2, 35].

6.1. Coupled system of NV center and nuclear spins. NV centers have shown to be sensitive probes of their nuclear spin environment. The NV center interacts with the nuclear spins via the anisotropic hyperfine interaction given by

$$\mathcal{H}_{\rm hf} = \sum_j \mathbf{S}\cdot\mathbf{A}^{(j)}\cdot\mathbf{I}_j = \sum_j \frac{g}{r_N^3}\left[3(\mathbf{S}\cdot\mathbf{r}_N)(I_j\cdot\mathbf{r}_N) - \mathbf{S}\cdot\mathbf{I}\right], \quad [27]$$

where $g = \frac{\hbar\mu_0\gamma_N\gamma_e}{4\pi}$, with the gyromagnetic ratios of nuclear and electron spins respectively γ_N and γ_e, and the vector $\vec{\mathbf{r}}_N^{(j)} = (r_{xj}, r_{yj}, r_{zj})$ joins the center of the NV and the nuclear spin [36, 37]. In the presence of a magnetic field, one can consider on the NV the pseudo two level system formed by the $\{0,-1\}$ levels. Applying now a secular approximation and retaining terms that commute with S_z gives $\mathcal{H}_{\rm hf} = \sum_j \frac{g_N}{(r_N^{(j)})^3} S_z\left[3r_z(r_{xj}I_{xj} + r_{yj}I_{yj}) + (3r_{zj}^2 - 1)I_{zj}\right]$. The overall Hamiltonian of the coupled system is then,

$$\mathcal{H} = \Delta S_z + |0\rangle\langle 0|\, H_{|0\rangle} + |-1\rangle\langle -1|\, H_{|-1\rangle} \quad [28]$$

with $\Delta = \Delta_0 - \gamma_e B_z$, where $\Delta_0 = 2.87$GHz is the zero field NV splitting, and

$$H_{|0\rangle} = \omega_L I_{zj} \quad [29]$$

$$H_{|-1\rangle} = \left[(\omega_L + A_{zz}^{(j)})I_{zj} + A_{zx}^{(j)}I_{xj} + A_{zy}^{(j)}I_{yj}\right] \quad [30]$$

represent the effective nuclear spin Hamiltonians conditioned on the state of the NV. Here, we have used the common spectroscopic notation [38], $A_{zz}^{(j)} = (3r_{zj}^2 - 1), A_{zx}^{(j)} = 3r_{zj}r_{xj}, A_{zy}^{(j)} = 3r_{zj}r_{yj}$ to represent the magnitude of the hyperfine interactions to spin j, that are contained in the hyperfine tensor $\mathbf{A}^{(j)} = A_{\mu,\nu}^{(j)}$.

^{14}N spin sensing. In the main paper we applied quantum interpolation to study the lineshape from a single ^{14}N spin intrinsic to the NV center.

The Hamiltonian of this coupled system is slightly different than what presented above,

$$\begin{aligned} \mathcal{H} &= \mathcal{H}_0 + V \quad [31]\\ \mathcal{H}_0 &= \Delta_0 S_z^2 + B_z(\gamma_e S_z + \gamma_N I_z) + P I_z^2 + A_\parallel S_z I_z \\ V &= \gamma_e B_\perp S_x + \frac{A_\perp}{2}(S_+ I_- + S_- I_+), \end{aligned}$$

with $A_\perp = -2.62$MHz, and where $\Delta = \Delta_0 - \gamma_e B_z$ is the resonance frequency of the NV center, and $\omega = P - A_\parallel/2 - \gamma_n B_z$, with the quadrupolar interaction $P = -4.95$MHz, the parallel hyperfine term $A_\parallel = -2.16$MHz, and the gyromagnetic ratio $\gamma_n = 0.31$kHz/G. In particular, the terms A_{zx}, A_{zy} that usually gives rise to the signal are missing.

However, we performed experiments close to the ground state anti-crossing of the NV center, $B_z \approx 1000$G, where due to the presence of a weak misaligned magnetic field, one obtains a term $\propto S_z I_x$. This term originates from second order perturbation effects due to a combination of the non-secular terms $B_\perp S_x$ and $\frac{A_\perp}{2}(S_+I_- + S_-I_+)$ that yield and effective transverse hyperfine coupling $A_{zx} \propto \frac{\gamma_e B_\perp A_\perp N}{\Delta\,\omega}$. The signal thus becomes stronger close to the avoided crossing, where the energy denominator Δ becomes small and the effective A_{zx} is larger.

6.2. NV nuclear spin sensing from a geometric perspective. In the sensing pulse sequences, the NV is prepared initially in the state $|\psi\rangle = \frac{1}{\sqrt{2}}(|0\rangle + |-1\rangle)$, while given the low magnetic field and high temperature, the nuclear spins are in the mixed state $\mathbb{1}_j/2$. Due to different evolutions of the nuclear spins conditioned on the $|0\rangle$ or $|-1\rangle$ of the NV center (following Eq. (28)), the evolution in the two NV manifolds gives rise to a destructive interference that is detected as a an apparent decay of the NV coherence.

We now provide a geometric perspective to spin sensing sequences with the aim of describing the origin of the increasing sensitivity and the decreasing linewidth with the number of cycles N.

We first define the unitary rotation operator $\mathcal{R}^j(\Theta_j, \hat{\mathbf{n}}_j) \equiv e^{-i\Theta_j\vec{\sigma}^j\cdot\hat{\mathbf{n}}_j/2}$, describing a rotation of the *nuclear* spin j around the axis $\hat{\mathbf{n}}_j$ by an angle Θ_j (the *flip* angle).

The fundamental units of the CPMG and XY8 spin sensing sequences are described by a unitary transformation composed of three successive rotations

$$\mathcal{U}_{\rm tot} \equiv \mathcal{R}(\Theta_a, \hat{\mathbf{n}}_a)\,\mathcal{R}(\Theta_b, \hat{\mathbf{n}}_b)\,\mathcal{R}(\Theta_a, \hat{\mathbf{n}}_a), \quad [32]$$

that, in turn, can be described as a rotation about a new rotation axis $\hat{\mathbf{n}}_{\rm tot}$ by a flip angle $\Theta_{\rm tot}$, $\mathcal{U}_{\rm tot} = e^{i\phi_{\rm tot}}\,\mathcal{R}(\Theta_{\rm tot}, \hat{\mathbf{n}}_{\rm tot})$, where $\phi_{\rm tot}$ is an unimportant global phase. Some algebra yields the total effective flip angle

$$\Theta_{\rm tot} = 2\arccos\left(\left|2b\cos\left(\frac{\Theta_a}{2}\right) - \cos\left(\frac{\Theta_b}{2}\right)\right|\right) \quad [33]$$

and the effective rotation axis

$$\mathbf{n}_{\rm tot} = 2b\sin\left(\frac{\Theta_a}{2}\right)\hat{\mathbf{n}}_a + \sin\left(\frac{\Theta_b}{2}\right)\hat{\mathbf{n}}_b \quad [34]$$

with

$$b = \cos\left(\frac{\Theta_a}{2}\right)\cos\left(\frac{\Theta_b}{2}\right) - (\hat{\mathbf{n}}_a\cdot\hat{\mathbf{n}}_b)\sin\left(\frac{\Theta_a}{2}\right)\sin\left(\frac{\Theta_b}{2}\right). \quad [35]$$

For CPMG-like sequences, the rotation axis associated with $\mathcal{U}_{\rm tot}$ lies in the plane spanned by the original rotation axes $\hat{\mathbf{n}}_a$ and $\hat{\mathbf{n}}_b$, i.e. $\hat{\mathbf{n}}_{\rm tot}$ always has the same azimuth angle as $\hat{\mathbf{n}}_b$ if we choose a coordinate system with $\hat{\mathbf{z}} = \hat{\mathbf{n}}_a$. We shall use this property later to visualize trajectories of metrology Hamiltonians in a three-dimensional visualization in Fig. S5. This is not the case for periodic dynamical decoupling sequences[39] (such as the spin echo[5]).

We can now use these results for the system described in Sec. 6.5.2, where the two axes of rotations are defined by the Hamiltonians $H_{|0,1\rangle}$ in Eq. (30).

Here we chose the coordinate system such that $\mathbf{z} = \hat{\mathbf{n}}_0$, i.e. the z-axis is aligned with the external magnetic field.

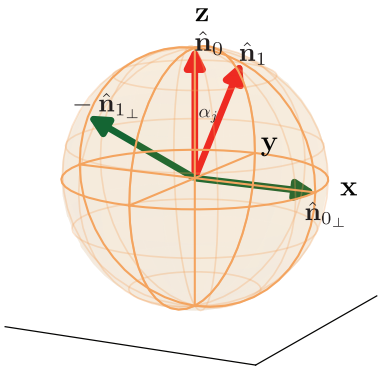

Fig. S16. Geometry of interferometric CPMG sensing. Bloch sphere description of the simple interferometric CPMG control sequence that is employed for sensing nuclear spins in the environment of an NV center. Here $\hat{\mathbf{n}}_0$ and $\hat{\mathbf{n}}_1$ are the two axes of the nuclear spin conditioned on the state of the NV. At the signal peak, obtained for $2\tau \approx \pi/\omega_L$, the result of the sequence are the two effective axes $\hat{\mathbf{n}}_{0_\perp}$ and $-\hat{\mathbf{n}}_{1_\perp}$ (see Eq. (36)).

We consider the coupling of the NV with a single spin j at a time, which furthermore allows us to choose the coordinate system such that $\phi_j = 0$ and the hyperfine coupling $C_j = 0$. Specifically, using the geometric notation [40] to represent the normalized Hamiltonians in Eq. (30), we have $\hat{H}_{|0\rangle} = \hat{\mathbf{n}}_0 = \mathbf{z}$ and $\hat{H}^j_{|-1\rangle} = \hat{\mathbf{n}}_1 = \cos(\alpha_j)\mathbf{z} + \sin(\alpha_j)\mathbf{z}_{j\perp}$, where $\mathbf{z}_{j\perp} = \cos(\phi_j)\mathbf{x} + \sin(\phi_j)\mathbf{y}$. We refer to the angle $\alpha_j = \tan^{-1}\left[\frac{A^{(j)}_{zx}}{\omega_L + A^{(j)}_{zz}}\right]$ as the *tilt* angle of spin j.

The simplest protocol for spin sensing is the interferometric CPMG-N technique [41, 42], which consists of $2N$ refocusing π pulses. For spin sensing, we sweep the delay between pulses 2τ, and the sensing signal dip appears when $2\tau \approx \pi/\omega_L$. At this time, the nuclear spin sees two different evolutions conditioned on the state of the NV center, that for $\omega_L \gg A_{zz}, A_{zx}$ can be approximated as

$$\begin{aligned}\mathcal{U}_{|0\rangle} &= \mathcal{R}(\pi/2, \hat{\mathbf{n}}_0)\mathcal{R}(\pi, \hat{\mathbf{n}}_1)\mathcal{R}(\pi/2, \hat{\mathbf{n}}_0) = \mathcal{R}(\hat{\mathbf{n}}_{|0\rangle}, \Theta_{|0\rangle}) \\ \mathcal{U}_{|-1\rangle} &= \mathcal{R}(\pi/2, \hat{\mathbf{n}}_1)\mathcal{R}(\pi, \hat{\mathbf{n}}_0)\mathcal{R}(\pi/2, \hat{\mathbf{n}}_1) = \mathcal{R}(\hat{\mathbf{n}}_{|-1\rangle}, \Theta_{|1\rangle}).\end{aligned} \quad [36]$$

(see Sec. 6.3 for the exact expression.) The effective axes of rotation are

$$\hat{\mathbf{n}}_{|0\rangle} = \frac{\hat{\mathbf{n}}_0 - \hat{\mathbf{n}}_1 \cos\alpha_j}{\sin\alpha_j} = -\hat{\mathbf{n}}_{1_\perp} \quad [37]$$

$$\hat{\mathbf{n}}_{|1\rangle} = \frac{\hat{\mathbf{n}}_1 - \hat{\mathbf{n}}_0 \cos\alpha_j}{\sin\alpha_j} = \hat{\mathbf{n}}_{0_\perp}. \quad [38]$$

Note that both axes lie in the plane span($\hat{\mathbf{n}}_0$, $\hat{\mathbf{n}}_1$) and are orthogonal to $\hat{\mathbf{n}}_1$ and $\hat{\mathbf{n}}_0$ respectively. Thus they retain the same mutually spanned angle $\hat{\mathbf{n}}_0 \cdot \hat{\mathbf{n}}_1 = \cos\alpha_j$ in magnitude. The effective flip angles are found to be $\Theta_{|0\rangle} = \Theta_{|-1\rangle} = (2\alpha_j)$, which leads to the to a simple *geometric* interpretation (see Fig. S16): effectively the control protocol translates the initial tilt angle α_j to twice the *flip* angle, while the effective axes are perpendicular to the initial axes are still separated by α_j.

We can now formally derive the dip signal from a CPMG/XY8 experiment[1], and interpret it geometrically using Eq. (36). The time evolution operator for the entire control sequence with N cycles is

$$U = |0\rangle\langle 0| \otimes \mathcal{U}^N_{|0\rangle} + |-1\rangle\langle -1| \otimes \mathcal{U}^N_{|-1\rangle}, \quad [39]$$

Note that for $\mathcal{U}^N_{|0/-1\rangle} = \mathcal{R}(N\Theta_{|0\rangle}, \hat{\mathbf{n}}_{|0\rangle})$ the rotation angles are amplified by N, whereas the rotation axes remain unchanged.

Initially, we prepare the NV in the $\frac{|0\rangle+|-1\rangle}{\sqrt{2}}$ state by applying a $\frac{\pi}{2}$ pulse. The initial state of the system is thus described by the density matrix $\rho_{\rm ini} = \frac{1}{4}(\mathbb{1} + \sigma_x) \otimes \mathbb{1}$, where the first operator acts on the NV space and the second on the nuclear spin space. After the decoupling pulse sequence, the system is thus in the state

$$\rho_{\rm final} = U\rho_{\rm ini}U^\dagger = \frac{1}{4}(\mathbb{1} + U(\sigma_x \otimes \mathbb{1})U^\dagger). \quad [40]$$

After the sequence, another $\frac{\pi}{2}$ pulse is applied, which maps the phase onto a population of the NV state. We can therefore define the signal as the expectation value $S = \langle\sigma_x \otimes \mathbb{1}\rangle$ before the last $\frac{\pi}{2}$ pulse. The signal can be interpreted as the overlap of the initial and final density matrix

$$S = \mathrm{Tr}(\sigma_x \otimes \mathbb{1}\rho_{\rm final}) = 4\mathrm{Tr}(\rho^\dagger_{\rm ini}\rho_{\rm final}) - 1. \quad [41]$$

Using Eq. (39) and Eq. (40), a straightforward calculation yields

$$\begin{aligned}S &= \frac{1}{4}\mathrm{Tr}[(\sigma_x \otimes \mathbb{1})(|0\rangle\langle -1| \otimes \mathcal{U}^N_{|0\rangle}{\mathcal{U}^N_{|-1\rangle}}^\dagger + |-1\rangle\langle 0| \otimes \mathcal{U}^N_{|-1\rangle}{\mathcal{U}^N_{|-0\rangle}}^\dagger)] \\ &= \frac{1}{4}\mathrm{Tr}(\mathcal{U}^N_{|0\rangle}{\mathcal{U}^N_{|-1\rangle}}^\dagger + \mathcal{U}^N_{|-1\rangle}{\mathcal{U}^N_{|-0\rangle}}^\dagger).\end{aligned} \quad [42]$$

Since the trace of any SU(2) rotation operator is real, the last two terms are equal and the signal can be expressed in geometric terms

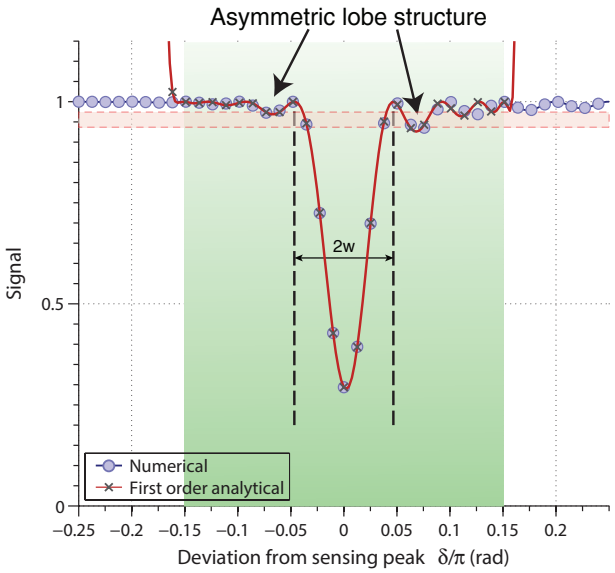

Fig. S17. Lineshape in spin sensing experiments. Here we compare the analytic expressions for the lineshape of spin sensing experiments with the numerically obtained result for a small deviation δ about the sensing peak. We considered $\alpha_j = 0.1$ rad and $N = 10$ cycles of the CPMG experiment. The result demonstrates that the first order expression obtained in Eq. (48) does indeed capture the lineshape accurately, including the asymmetry in the sidelobes on either side of the sensing peak (red dashed lines). The green shading represents the region over which the first order expression is a good approximation. The dashed lines describe the evaluation of the signal linewidth w following Eq. (49).

[1] CPMG and XY8 sequences just differ in the phases of the pulses employed, and the resulting signal in both cases is quantitatively the same.

$$S = \frac{1}{2}\mathrm{Tr}\Big\{\Big[\mathbb{1}\cos\Big(\frac{N\Theta_{|0\rangle}}{2}\Big) - i\hat{\mathbf{n}}_{|0\rangle}\cdot\boldsymbol{\sigma}\,\sin\Big(\frac{N\Theta_{|0\rangle}}{2}\Big)\Big] \times \Big[\mathbb{1}\cos\Big(\frac{N\Theta_{|-1\rangle}}{2}\Big) - i\hat{\mathbf{n}}_{|-1\rangle}\cdot\boldsymbol{\sigma}\,\sin\Big(\frac{N\Theta_{|-1\rangle}}{2}\Big)\Big]\Big\} = 1 - \sin^2(N\alpha_j)\cos^2(\alpha_j/2) \quad [43]$$

To obtain the last line, we used $(\hat{\mathbf{n}}_{|0\rangle}\cdot\boldsymbol{\sigma})(\hat{\mathbf{n}}_{|-1\rangle}\cdot\boldsymbol{\sigma}) = \hat{\mathbf{n}}_{|0\rangle}\cdot\hat{\mathbf{n}}_{|-1\rangle}\mathbb{1} + i\boldsymbol{\sigma}\cdot(\hat{\mathbf{n}}_{|0\rangle}\times\hat{\mathbf{n}}_{|-1\rangle})$ and $\mathrm{Tr}(\sigma_j) = 0$ for all terms containing a single Pauli matrix.

Geometrically, the signal in Eq. (43) is just the overlap of the rotations $\mathcal{U}^N_{|0\rangle} = \mathcal{R}(N\alpha_j, -\hat{\mathbf{n}}_{1_\perp})$ and $\mathcal{U}^N_{|-1\rangle} = \mathcal{R}(N\alpha_j, \hat{\mathbf{n}}_{0_\perp})$. It also becomes evident that amplification of the flip angle from α_j to $N\alpha_j$ upon application of N cycles explains why the peak signal intensity grows quadratically with the number of cycles N – an important feature for external spin sensing. Equivalently, the application of N cycles leads to a longer evolution path length and hence larger phase accumulation in the interferometric detection.

6.3. Exact analysis of the signal dip. To evaluate the exact expression for the peak signal from a CPMG/XY8 experiment we consider the propagators $\mathcal{U}_{|0\rangle} = \mathcal{R}(\eta\pi/2, \hat{\mathbf{n}}_1)\mathcal{R}(\pi, \hat{\mathbf{n}}_0)\mathcal{R}(\eta\pi/2, \hat{\mathbf{n}}_1)$, and $\mathcal{U}_{|-1\rangle} = \mathcal{R}(\pi/2, \hat{\mathbf{n}}_0)\mathcal{R}(\eta\pi, \hat{\mathbf{n}}_1)\mathcal{R}(\pi/2, \hat{\mathbf{n}}_0)$, where $\eta = \Big[\big(1+\frac{A_{zz}}{\omega_L}\big)^2 + \big(\frac{A_{zx}}{\omega_L}\big)^2\Big]^{1/2}$ takes into account that the nuclear spin Hamiltonian norm in the two NV manifolds is different.

This gives for N cycles of the experiment,

$$\mathcal{U}^N_{|0\rangle} = -\mathbb{1}\cos N\alpha_j + i\frac{\sin N\alpha_j}{\sin\alpha_j}\boldsymbol{\sigma}\cdot [-\hat{\mathbf{n}}_{1_\perp}\sin\alpha_j + \hat{\mathbf{n}}_1\cos\alpha_j\cos(\eta\pi/2)] \quad [44]$$

$$\mathcal{U}^N_{|-1\rangle} = -\mathbb{1}\cos N\alpha_j + i\frac{\sin N\alpha_j}{\sin\alpha_j}\boldsymbol{\sigma}\cdot [\hat{\mathbf{n}}_{0_\perp}\sin\alpha_j\sin(\eta\pi/2) + \hat{\mathbf{n}}_0\cos(\eta\pi/2)]\,,$$

where $\cos(\alpha_j) = \cos(\alpha_j)\sin(\eta\pi/2)$. Note that when the interactions are weak, $\omega_L \gg A_{zz}, A_{zx}$, we have $\eta \to 1$ and $\cos\alpha_j \to \cos\alpha_j$, and one exactly recovers the expressions Eq. (36) above. The exact signal including the hyperfine terms is now,

$$1 - S = \cos^2(N\alpha_j) + \frac{\sin^2(N\alpha_j)}{\sin^2\alpha_j}\big[\sin^2\alpha_j\cos^2\alpha_j\,(\cos(\eta\pi/2) - 1) + \cos^2\alpha_j - \cos^2\alpha_j + \sin^2\alpha_j\cos(\eta\pi/2)\big]$$

6.4. Linewidth of the nuclear spin sensing signal. The previous sections considered the peak signal obtained as a result of the spin sensing experiment. However, it is also of critical importance to quantify the linewidth of the sensing signal since by falling as $1/N$ it allows sensing spins at higher resolution as N increases.

To derive the sensing linewidth, we resort to an expansion in the deviation δ about the signal peak obtained in Eq. (36),

$$\mathcal{U}^N_{|0\rangle}(\pi+\delta) = [\mathcal{R}(\pi/2+\delta, \hat{\mathbf{n}}_0)\mathcal{R}(\pi+2\delta, \hat{\mathbf{n}}_1)\mathcal{R}(\pi/2+\delta, \hat{\mathbf{n}}_0)]^N \quad [45]$$

$$\approx \mathbb{1}\cos(N\alpha'_j) + i\frac{\sin(N\alpha'_j)}{\sin\alpha'_j}\boldsymbol{\sigma}\cdot[-\hat{\mathbf{n}}_{1_\perp}\sin\alpha_j - \delta(1+\cos\alpha_j)\hat{\mathbf{n}}_1]$$

where to first order in δ,

$$\sin^2\alpha'_j = \sin^2\alpha_j + \delta^2(1+\cos\alpha_j)^2\,. \quad [46]$$

which incorporates an effective destructive interference in the flip angle. It is also instructive to compare Eq. (45) with Eq. (36): the expressions are identical except for a corruption factor proportional to δ in Eq. (45). This can be visualized as a slight mixing of the perfect vector $\hat{\mathbf{n}}_{1_\perp}$ with a term $\delta(1+\cos\alpha_j)\hat{\mathbf{n}}_1$. Crucially this is the same factor that causes the interference in Eq. (46). Similarly in the $|-1\rangle$ manifold of the NV center one has,

$$\mathcal{U}^N_{|-1\rangle}(\pi+\delta) = [\mathcal{R}(\hat{\mathbf{n}}_1, \pi/2+\delta)\mathcal{R}(\hat{\mathbf{n}}_0, \pi+2\delta)\mathcal{R}(\hat{\mathbf{n}}_1, \pi/2+\delta)]^N \quad [47]$$

$$\approx \mathbb{1}\cos(N\alpha'_j) + i\frac{\sin(N\alpha'_j)}{\sin\alpha'_j}\boldsymbol{\sigma}\cdot[\hat{\mathbf{n}}_{0_\perp}\sin\alpha_j - \delta(1+\cos\alpha_j)\hat{\mathbf{n}}_0]$$

This gives the signal similar to Eq. (43), but now as a function of the deviation from the sensing peak δ,

$$S = \cos^2(N\alpha'_j) + \frac{\sin^2(N\alpha'_j)}{\sin^2\alpha'_j}\big[-\sin^2\alpha_j\,\cos\alpha_j + \delta^2\cos\alpha_j\,(1+\cos\alpha_j)^2 - 2\delta\sin^2\alpha_j\,(1+\cos\alpha_j)\big] \quad [48]$$

Figure S17 compares the analytical expression in Eq. (48) to an exact numerical calculation. It is evident that for most of the region close to the sensing peak (shaded region), the agreement is very close.

Importantly then the insight offered by Eq. (45) allows one to intuitively understand the origin of the sensing linewidth: with increasing δ, there is destructive interference of the flip-angle α_j to α'_j (Eq. 46). As the number of cycles is increased, the destructive interference effect is magnified by N (Eq. 48) and leads to a decreasing linewidth $\propto 1/N$.

To quantify the linewidth w exactly, let us define it as the first *zero* of sensing signal S in Eq. (48). This happens when the function $\sin(N\alpha'_j)$ vanishes, i.e. $\alpha'_j = \pi/N$, giving the linewidth in units of *angle*,

$$w^2 \approx \frac{\sin^2(\pi/N) - \sin^2\alpha_j}{2\cos^2(\alpha_j/2)} \quad [49]$$

Similarly, the sensing linewidth in units of time can be evaluated as w/ω_L, giving for small α_j,

$$w/\omega_L \approx 1/(\sqrt{2}\omega_L\cos(\alpha_j/2))\cdot\sin(\pi/N) \quad [50]$$

that indeed falls as $\propto 1/N$ as we would expect for interferometric detection.

The linewidth directly shows the origin of the *asymmetry* of the sensing peak. This is subtle feature, characteristic of CPMG-like sequences (but not of period sequences) that we are able to discern clearly in our experiments via quantum interpolation (Fig. 1 of main paper and Fig. S18). This shows that our quantum interpolation expansion is indeed of low error and faithfully represents the true signal.

The asymmetry is manifested by the linear term in δ in Eq. (48), or equivalently the odd $\sin\delta$ term in Eq. (48), as it is evident in Fig. S17. Indeed, the time $2\tau = \pi/\omega_L$ is not the exact signal minimum; instead, at this time, the effective vectors $[\hat{\mathbf{n}}_{0_\perp}\sin(\alpha) - \delta(1+\cos\alpha)\hat{\mathbf{n}}_0]$ and $[-\hat{\mathbf{n}}_{1_\perp}\sin\alpha - \delta(1+\cos\alpha)\hat{\mathbf{n}}_1]$ in Eq. (45) and Eq. (47) are not exactly perpendicular to each other away from the sensing peak.

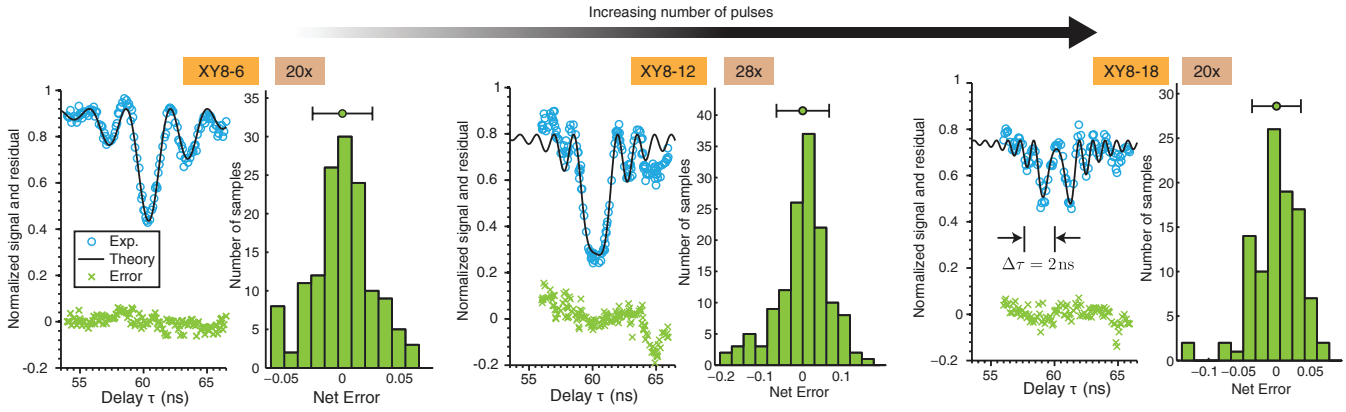

Fig. S18. Detailed analysis of ^{14}N spin sensing experiments. In these panels we study the lineshape of the signal from a ^{14}N supersampled via quantum interpolation. This data was also depicted in Fig. 1.**B** of the main paper. Here the experimental data (points) is fit to the expected theoretical lineshape (solid line) that is slight asymmetric. The experiments were performed at 954.71G, and from the model we extract the misalignment value of 1.14G. The crosses denote the total error of each sample from the theoretical result. The right panels show a histogram of the errors of different supersamples. The hardware resolution here was $\Delta\tau = 2$ns, and we effectively supersampled by the factors denoted by the x-. We sweep the number of XY8-N cycles from left to right, and the lineshape opens up characteristic sidebands upon increasing number of pulses. We find that the signal obtained via quantum interpolation is indeed a faithful representation, with the error under a few percent.

6.5. Experimental Magnetometry via Quantum Interpolation.

In this section we provide additional information for the experiments described in the main paper, including details of the theoretical models in the fits.

6.5.1. ^{14}N spin sensing and lineshape analysis. In the main paper we applied quantum interpolation based supersampling to study the lineshape from a single ^{14}N spin intrinsic to the NV center. We performed experiments close to the ground state anti-crossing of the NV center, $B_z \approx 1000$G, where due to the presence of a weak misaligned magnetic field, one obtains a peak signal under XY8-N of the form

$$S(\delta = 0) = \cos(8N\alpha), \quad \text{where } \alpha = \tan^{-1}\left[\frac{\gamma_e B_\perp A_\perp}{\Delta\,\omega}\right], \quad [51]$$

with $A_{xx} = -2.62$MHz, and where $\Delta = \Delta_0 - \gamma_e B_z$ is the resonance frequency of the NV center, and $\omega = P - A_\parallel/2 - \gamma_n B_z$, with the quadrupolar interaction $P = -4.95$MHz, the parallel hyperfine term $A_\parallel = -2.16$MHz, and the gyromagnetic ratio $\gamma_n = 0.31$kHz/G. As explained above, this signal originates from second order perturbation effects due to a combination of the transverse field $B_\perp S_x$ and the hyperfine $A_\perp$. The signal becomes stronger close to the avoided crossing. For typical values of misaligned fields, α is small, and the signal is approximately $S \propto \cos\left[\frac{8\gamma_e B_\perp A_\perp N}{\Delta\,\omega}\right]$.

In Fig. 1.**B-C** of the main paper, and in Fig. S18 we perform XY8-N sensing while sweeping the number of cycles N. In Fig. S18 we fit the data to the theoretical lineshape, numerically evaluated following Eq. (43), where the operators $\mathcal{U}_{|0\rangle}$ and $\mathcal{U}_{|1\rangle}$ are now defined with the tilt angle $\alpha_j = \alpha$ from Eq. (51) above. We find a remarkable match with the theoretical model in Fig. S18, and from the data we extract a value of $B_\perp$ which corresponds to an misalignment of 1.14G at the bare field of 954.71G. One is also able to discern the asymmetry in the lineshape (see Sec. 6.4).

6.5.2. Data fitting and error estimation. To fit the theoretical model to the data, we use a steepest descent minimization algorithm to minimize the χ^2 in conjunction with simulated annealing to avoid local minima and ensure the global best fit. Subsequently, we use a Monte-Carlo approach to estimate the uncertainty of the various fit parameters.

Let us denote the fit parameters for our model by $\mathbf{P}$. For a given set $\mathbf{P}$, our theoretical model provides a non-linear functional relation $y = f(x|\mathbf{P})$. Given a measured set of data points $\{x_n\}$ and $\{y_n\}$, we determine the optimal set of parameters $\mathbf{P}_{\rm opt}$ by minimizing $\chi^2 = \sum_n [y_n - f(x_n|\mathbf{P})]^2/\sigma_y^2$. Here we have assumed that the statistical error σ_y of the measured data points is identical for all points.

For example, the fitting parameters for Fig. 3 in the main article are the tilt angle α_1 of the rotation axis of $\mathcal{U}(\tau_{k+1})$, as well as the offsets and scaling factors for both the x and y axes (x and y corresponding to deviation time from the sensing

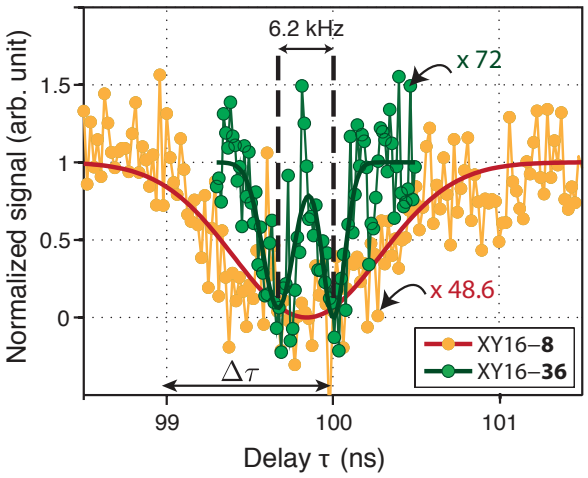

Fig. S19. Quantum interpolation for increasing resolution. Here we demonstrate that quantum interpolation while increasing the number of pulses can allow us to resolve peaks that were normally indistinguishable. We perform AC magnetometry from two distinct incoherent sources, separated by 6.2kHz (see also Fig. 2.**B** of main paper). The timing resolution here experiments was $\Delta\tau = 1$ns, and without quantum interpolation based supersampling, the entire data would just consist of four points in this plot. The supersampling resolution gains for both experiments are indicated in the boxes. Note that we have normalized the two experimental results so that the peak signal strength is identical for both cases.

peak and the measured signal intensity in this case).

Once $\mathbf{P}_{\rm opt}$, the statistical uncertainty of y_m is estimated from the deviation from the optimally fitted function $\sigma_y^2 \approx \sum_n [y_n - f(x_n|\mathbf{P}_{\rm opt})]^2/(N-1)$, where N is the number of data points. The value of σ_y obtained by this procedure yields sets a lower bound for the true statistical uncertainty, as any systematic deviation of the fitted function (i.e. if we have not captured the underlying true functional form in our theoretical model) increases σ_y. Subsequently the uncertainty in the fit parameters $\mathbf{P}$ can be estimated beyond linear order by generating artificial data sets of points $\{x_n\}$ and $\{y_n\}$ statistically distributed around $f(x_n|\mathbf{P}_{\rm opt})$, subsequently performing a fit for each data set. We assume a Gaussian distribution for the generation of these data points, an assumption which can be verified by inspecting the distribution of $\delta y_n = y_n - f(x_n|\mathbf{P}_{\rm opt})$ in the original data. Repeating this procedure yields a distribution of fit parameters of which the distributional form, confidence intervals and standard deviation for the individual parameters can be extracted.

6.5.3. Spectroscopy of Classical AC Magnetic Fields. As a supplemental experiment to the AC magnetometry experiments described in Fig. 2.**B** of the main paper, we performed magnetometry of two AC signals separated by 6.2kHz with XY16-8 and XY16-36 (see Fig. S19). We observe that the two peaks cannot be resolved by XY16-8, but upon increasing the number of pulses, one is able to resolve them. It is important to note that we employed quantum interpolation for both experiments; indeed given our timing resolution of $\Delta\tau = 1$ns, the entire data in Fig. S19 would otherwise just consist of four points.

The experiment in Fig. S19, along with those in Fig. 2 of the main paper demonstrate that via quantum interpolation, the effective ability to resolve two closeby spectral frequencies is no longer limited by hardware but only by the number of pulses that can be reliably applied.

7. Code for the construction of the optimal supersampling sequence

Here we present a simple code (in MATLAB) that allows constructing the optimal interpolation sequence for a desired sampling time $q/(p+q)\Delta\tau$ (see Fig. S10). The algorithm yields an array of time delays for how the basic CPMG building blocks $\mathcal{U}(\tau_k)$ and $\mathcal{U}(\tau_{k+1})$ (each consisting of 3 rotations) should be ordered and the π-pulses phases chosen according to the XY8 scheme.

Fig. S20. Matlab code for the optimal quantum interpolation sequence construction

```
%% Basic blocks of delay time (separation between neighbouring pi pulses).

U_0 = [tau, 2*tau, tau];
U_1 = [tau+delta_tau, 2*(tau+delta_tau), tau+delta_tau];
% tau is the parameter we sweep in experiment and delta_tau is the smallest time step we can
    sweep by

%% Assemble the delay time in the order as in the optimal construction of a supersampling
    sequence.

delay={}; % Initialize cell array 'delay'
count=0; m=0;

for  j = 1: 4*n  %  Here n is XY8 cycle number
       m = m + sample;
   % sample is a fraction number between 0 and 1, rounded to multiples of 1/(4*n);
      if abs(m) <= 1/2
          count = count+1;
          delay{count} = U_0;
      else
          count  = count+1;
          delay{count} = U_1;
          m = m-1;
      end
end

% For instance, for n=1 and sample =1/4, one gets a delay cell array: delay={U_0 U_0 U_1 U_0}.

% Let us take as given functions which add a pulse or delay to a sequence.
% For simplicity, the carrier power and frequency are not shown as inputs and only phase is
    emphasized here.

function add_pi/2_pulse(phase)
function add_pi_pulse(phase)
function add_delay(delay_time)

%% Create a supersampling XY8-n sequence, combining pi pulses with correct phase and delay.

add_pi/2_pulse(0);

for j=1:4*n
 if mod(j,4)==1 || mod(j,4)==2
      add_delay(delay{j}(1,1));
      add_pi_pulse(0);  % pi|x
      add_delay(delay{j}(1,2));
      add_pi_pulse(90); % pi|y
      add_delay(delay{j}(1,3));
else
      add_delay(delay{j}(1,1));
      add_pi_pulse(90);  % pi|y
      add_delay(delay{j}(1,2));
      add_pi_pulse(0); % pi|x
      add_delay(delay{j}(1,3));
end
end

add_pi/2_pulse(0);
```

References

1. Degen CL, Poggio M, Mamin HJ, Rettner CT, Rugar D (2009) Nanoscale magnetic resonance imaging. *Proc. Nat Acad. Sc.* 106(5):1313–1317.
2. Taminiau TH et al. (2012) Detection and control of individual nuclear spins using a weakly coupled electron spin. *Phys. Rev. Lett.* 109(13):137602.
3. Kolkowitz S, Unterreithmeier QP, Bennett SD, Lukin MD (2012) Sensing distant nuclear spins with a single electron spin. *Phys. Rev. Lett.* 109:137601.
4. Pham LM et al. (2016) Nmr technique for determining the depth of shallow nitrogen-vacancy centers in diamond. *Phys. Rev. B* 93:045425.
5. Hahn EL (1950) Spin echoes. *Phys. Rev.* 80(4):580–594.
6. Nielsen MA (2002) A simple formula for the average gate fidelity of a quantum dynamical operation. *Physics Letters A* 303:249.
7. Baker H (1902). *Proc Lond Math Soc.*
8. Magnus W (1954) On the exponential solution of differential equations for a linear operator. *Communications on Pure and Applied Mathematics* 7(4):649–673.
9. Ajoy A, Cappellaro P (2012) Mixed-state quantum transport in correlated spin networks. *Phys. Rev. A* 85:042305.
10. London P et al. (2013) Detecting and polarizing nuclear spins with double resonance on a single electron spin. *Phys. Rev. Lett.* 111:067601.
11. Ajoy A, Bissbort U, Lukin MD, Walsworth RL, Cappellaro P (2015) Atomic-scale nuclear spin imaging using quantum-assisted sensors in diamond. *Phys. Rev. X* 5:011001.
12. Laraoui A, Meriles CA (2013) Approach to dark spin cooling in a diamond nanocrystal. *ACS Nano* 7(4):3403–3410. PMID: 23565720.
13. Hartman SR, Hahn EL (1962) Nuclear double resonance in the rotating frame. *Phys. Rev.* 128:2042–2053.
14. Pines A, Gibby MG, Waugh JS (1973) Proton-enhanced nmr of dilute spins in solids. *J. Chem. Phys.* 59(2):569–590.
15. Cai JM et al. (2012) Robust dynamical decoupling with concatenated continuous driving. *New J. Phys.* 14(11):113023.
16. Kong X, Stark A, Du J, McGuinness LP, Jelezko F (2015) Towards chemical structure resolution with nanoscale nuclear magnetic resonance spectroscopy. *Phys. Rev. Applied* 4:024004.
17. Ma W et al. (2015) Resolving remote nuclear spins in a noisy bath by dynamical decoupling design. *Physical Review A* 92(3):033418.
18. Ajoy A, Álvarez GA, Suter D (2011) Optimal pulse spacing for dynamical decoupling in the presence of a purely dephasing spin bath. *Phys. Rev. A* 83:032303.
19. Casanova J, Wang ZY, Haase J, Plenio M (2015) Robust dynamical decoupling sequences for individual-nuclear-spin addressing. *Physical Review A* 92(4):042304.
20. Viola L, Lloyd S (1998) Dynamical suppression of decoherence in two-state quantum systems. *Phys. Rev. A* 58:2733.
21. Cywiński L, Witzel WM, Das Sarma S (2009) Electron spin dephasing due to hyperfine interactions with a nuclear spin bath. *Phys. Rev. Lett.* 102:057601.
22. Álvarez GA, Ajoy A, Peng X, Suter D (2010) Performance comparison of dynamical decoupling sequences for a qubit in a rapidly fluctuating spin bath. *Phys. Rev. A* 82:042306.
23. Paz-Silva GA, Viola L (2014) General transfer-function approach to noise filtering in open-loop quantum control. *Phys. Rev. Lett.* 113:250501.
24. Ajoy A, Cappellaro P (2013) Perfect quantum transport in arbitrary spin networks. *Phys. Rev. B* 87:064303.
25. Householder AS (1958). *J. Assoc. Comput. Mach.* 5(339).
26. Lovchinsky I et al. (2016) Nuclear magnetic resonance detection and spectroscopy of single proteins using quantum logic. *Science.*
27. Balasubramanian G et al. (2009) Ultralong spin coherence time in isotopically engineered diamond. *Nat. Mater.* 8(5):383–387.
28. Shi F et al. (2015) Single-protein spin resonance spectroscopy under ambient conditions. *Science* 347(6226):1135–1138.
29. Staudacher T et al. (2015) Probing molecular dynamics at the nanoscale via an individual paramagnetic centre. *Nature communications.*
30. Ernst R, Bodenhausen G, Wokaun A (1987) *Principles of nuclear magnetic resonance in one and two dimensions.* (Clarendon Press Oxford).
31. Van der Sar T, Casola F, Walsworth R, Yacoby A (2015) Nanometre-scale probing of spin waves using single-electron spins. *Nature Communications.*
32. Trifunovic L et al. (2015) Trifunovic, luka and pedrocchi, fabio l and hoffman, silas and maletinsky, patrick and yacoby, amir and loss, daniel. *Nature nanotechnology* 10(6):541–546.
33. Liu L et al. (2012) Spin-torque switching with the giant spin hall effect of tantalum. *Science* 336(6081):555–558.
34. Jelezko F, Wrachtrup J (2006) Single defect centres in diamond: A review. *Physica Status Solidi (A)* 203(13):3207–3225.
35. Kolkowitz S, Unterreithmeier QP, Bennett SD, Lukin MD (2012) Sensing distant nuclear spins with a single electron spin. *Phys. Rev. Lett.* 109(13):137601.
36. Childress L et al. (2006) Coherent dynamics of coupled electron and nuclear spin qubits in diamond. *Science* 314(5797):281–285.
37. Cai J, Jelezko F, Plenio MB, Retzker A (2013) Diamond-based single-molecule magnetic resonance spectroscopy. *New J. Phys.* 15(1):013020.
38. Abragam A (1961) *Principles of Nuclear Magnetism.* (Oxford Univ. Press).
39. Khodjasteh K, Lidar DA (2007) Performance of deterministic dynamical decoupling schemes: Concatenated and periodic pulse sequences. *Phys. Rev. A* 75(6):062310.
40. Ajoy A, Rao RK, Kumar A, Rungta P (2012) Algorithmic approach to simulate hamiltonian dynamics and an nmr simulation of quantum state transfer. *Phys. Rev. A* 85:030303.
41. Carr HY, Purcell EM (1954) Effects of diffusion on free precession in nuclear magnetic resonance experiments. *Phys. Rev.* 94(3):630–638.
42. Meiboom S, Gill D (1958) Modified spin-echo method for measuring nuclear relaxation times. *Rev. Sc. Instr.* 29(8):688–691.